



---

# **Level-Crossing and Multi-Quantum Spectra of Muoniated Radicals**

---

**Master's Thesis**

**by David Walk**

**Supervised by Dr. Andrin Doll**

**Examined by Prof. Dr. Gunnar Jeschke**

**Institute of Molecular Physical Science**

Zurich, February 4, 2026

## Abstract

Characterization of the muon species formed after implantation during muon spin resonance ( $\mu$ SR) experiments can give insights into different properties of the sample. Multiple techniques exist to examine coupled electron-muon centers, i.e. muonium (Mu) and its potential reactions. In this work, we investigated the applicability of avoided-level crossing (ALC) and multi-quantum (MQ)  $\mu$ SR to observe and characterize weakly-coupled Mu in powder samples. In weakly-coupled Mu, the electron is spatially separated from the muon and the main interaction is dipolar, whereas strong coupling occurs when the electron and muon wavefunctions overlap significantly, giving rise to a large isotropic hyperfine interaction. Numerical ALC simulations revealed that for weakly-coupled Mu, the resonances start overlapping with the muon repolarization, distorting and broadening the powder spectrum. This deems ALC- $\mu$ SR unviable, since the resulting spectra are hard to interpret. Zero-field (ZF), transverse field and MQ- $\mu$ SR measurements were conducted on a powder sample of the zeolite silicalite-1. The ZF- and MQ- $\mu$ SR measurements demonstrated that strongly-coupled Mu is formed after muon implantation, while weakly-coupled Mu is observed after  $t \approx 300$  ns. This suggests that reactions of the strongly-coupled Mu lead to the formation of weakly-coupled Mu. These results confirm the viability of MQ- $\mu$ SR for observing delayed formation of weakly-coupled Mu. The impact on MQ spectra of the angle between the interspin vector and the applied magnetic field, the isotropic muon-electron hyperfine coupling constant, the transverse electron relaxation time and the microwave irradiation amplitude were studied via numerical spin dynamics simulations. Finally, rotary spin echos were found to lead to a small, but significant, increase in absolute signal intensity and a relative increase of  $\approx 90\%$  compared to linear phase pulses for MQ- $\mu$ SR.

## Acknowledgments

I would like to thank Dr. Andrin Doll for sharing his extensive knowledge with me, always having the patience to answer my questions and for teaching me invaluable lessons in both research and life in general. I am grateful to Prof. Dr. Gunnar Jeschke for supervising the thesis and thereby allowing me to pursue an external Master's thesis. I also sincerely appreciate the valuable feedback on this manuscript provided by Annina Weber and Mario Baumgartner.

# Contents

<b>1</b>	<b>Introduction</b>	<b>1</b>
<b>2</b>	<b>Theoretical Background</b>	<b>2</b>
2.1	Introduction to the $\mu$ SR experiment . . . . .	2
2.1.1	Comparison to other Magnetic Resonance Techniques . . . . .	4
2.1.2	Measurement Setup . . . . .	5
2.2	Muonium . . . . .	6
2.2.1	Strong and Weak Coupling Limit . . . . .	7
2.2.2	Zero-field Spectra . . . . .	9
2.2.3	Repolarization . . . . .	11
2.2.4	Avoided Level-Crossing Resonance . . . . .	11
2.2.5	Multi-Quantum Approach . . . . .	13
<b>3</b>	<b>Experimental</b>	<b>16</b>
3.1	Setup . . . . .	16
3.2	Sample Preparation . . . . .	17
3.3	Software . . . . .	17
<b>4</b>	<b>Results and Discussion</b>	<b>18</b>
4.1	Numerical ALC Simulations . . . . .	18
4.2	Limit of the Analytical ALC Model . . . . .	19
4.3	Parameter Dependence of Multi-Quantum Resonances . . . . .	21
4.3.1	$\theta$ -Dependence . . . . .	21
4.3.2	$A_{\text{iso}}$ -Dependence . . . . .	22
4.3.3	$T_2^{\text{e}^-}$ -Dependence . . . . .	23
4.3.4	$v_1$ -Dependence . . . . .	24
4.4	Muonium in Silicalite-1 . . . . .	25
4.5	Rotary Spin Echos . . . . .	27
<b>5</b>	<b>Conclusion &amp; Outlook</b>	<b>30</b>

# 1 Introduction

Muon spin rotation/relaxation/resonance ( $\mu$ SR) is a method adopted from particle physics that probes local magnetic properties via (anti-)muons  $\mu^\pm$ . The implanted muons are positively charged, allowing them to bind electrons  $e^-$ , forming electron-muon centers. These coupled electron-muon centers called muonium (Mu) are a bound state of a muon and an electron. They form during the thermalization process of the implanted muons, which enter the sample at rather high energies of 4–40 MeV. The muon energy is then reduced to 2–30 keV via ionization of atoms and scattering with electrons. This lowers the energy of the muon enough for it to capture an electron, forming Mu. Mu is a light analog of hydrogen  $H\left(\frac{m_\mu}{m_p} \approx \frac{1}{9}\right)$  [1] and therefore also a reactive radical, making a plethora of reactions possible in which the electron is lost again. This results in repeated formation and decay of Mu, further decreasing the muon energy to  $\approx 50$  eV. [2] Finally, collisions with atoms leads to the thermalized state, which can be a free muon, Mu or  $\text{Mu}^-$  (bound state consisting of  $\mu^+ e^- e^-$ , analogous to  $H^-$ ) [2].

For this work, the cases in which Mu is the thermalized state are relevant. Due to the high reactivity of Mu, further reactions can occur within a muon's lifetime, which leads to the delayed formation of a new muon species. The end product of these reactions is known as the final state. Several experimental radio-frequency (RF)  $\mu$ SR methods exist to characterize the final state. Cottrell et al. used RF techniques to examine the muon charge state conversion in silicon, showing that the thermalized Mu reacts to  $\mu^+$  as the final state [3]. In a different experiment, Dehn et al. explored the reaction of gold nanoparticles (GNPs) embedded in mesoporous silica [4]. Comparison to measurements on pure silica allowed them to conclude that the Mu reacts with the GNPs, losing its electron in the process. In contrast, the Mu stays intact in pure silica. Moreover, RF- $\mu$ SR has been successfully applied to characterize Mu present in the final state. McKenzie et al. examined the muoniated cyclohexadienyl radical ( $C_6H_6\text{Mu}$ ) [5], which is a good benchmark system as it has been studied previously [6, 7]. They determined the isotropic electron-muon hyperfine coupling constant to be  $A_{\text{iso}} = 514.74(4)$  MHz. This puts the Mu found in  $C_6H_6\text{Mu}$  well in the strong coupling regime, allowing the use of already established RF- $\mu$ SR techniques.

To date, to the best of our knowledge, no method exists to study powder samples in which the final state is weakly-coupled Mu. In weakly-coupled Mu, the anisotropic dipolar interaction dominates the electron-muon hyperfine interaction. A newly emerging technique to characterize weakly-coupled Mu is by driving formally forbidden transitions. This multi-quantum (MQ) approach was first introduced in Ref. [8] and is inspired by well-established electron paramagnetic resonance (EPR) methods that rely on driving forbidden MQ transitions [9]. An unpublished MQ- $\mu$ SR powder spectrum of strontium titanate ( $\text{SrTiO}_3$ ) is given in Fig. 1. The presence of the resonance is enough to confirm that a weakly-coupled Mu state is formed, as the peak is a result of driving MQ transitions, which is only possible in weakly-coupled Mu. Note, however, that  $\text{SrTiO}_3$  is a model system for the MQ approach, since the weakly-coupled Mu state that forms instantly after muon implantation has been identified previously with ordinary single-crystal  $\mu$ SR measurements [10, 11].

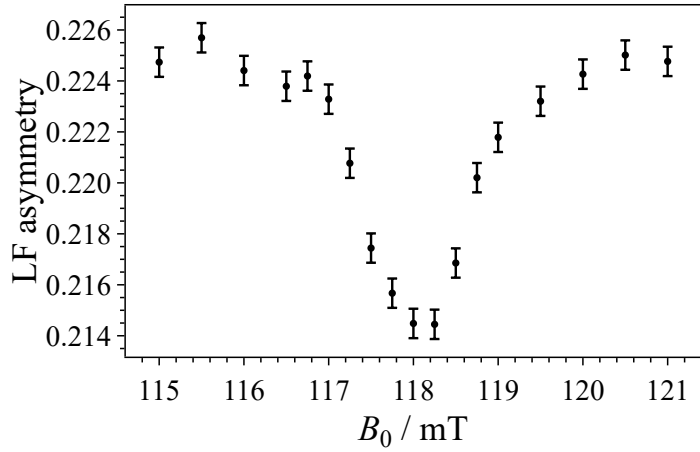


**Fig. 1:** Previously measured MQ- $\mu$ SR powder spectrum of SrTiO<sub>3</sub> at 17 K with a microwave irradiation frequency of  $\nu_{\mu\text{w}} = 3.335$  GHz. The peak at  $B_0 = 118$  mT is a result of driving MQ transitions, confirming the presence of weakly-coupled Mu with sufficiently large anisotropic electron-muon hyperfine coupling.

As the MQ- $\mu$ SR approach is still in its early stages, naturally, the theory is not fully developed, limiting the obtainable information from spectra. Furthermore there are potential improvements to be gained in the experimental approach. In this work, the feasibility of avoided-level crossing (ALC)  $\mu$ SR to characterize weakly-coupled Mu was studied using numerical spin dynamics simulations. Additional simulations were carried out to investigate the dependence of MQ transitions on the angle  $\theta$  between the interspin vector and the applied magnetic field. The MQ powder spectrum dependence on  $A_{\text{iso}}$ , the transverse electron relaxation time  $T_2^{\text{e}^-}$  and the microwave pulse amplitude  $\nu_1$  were analyzed. Additionally, the first experimental MQ- $\mu$ SR spectrum of the zeolite silicalite-1 (S-1) is reported, establishing that a chemical reaction to a weakly-coupled Mu state occurs. Finally, potential advantages of utilizing rotary echos instead of linear phase pulses for MQ excitation during MQ- $\mu$ SR experiments were studied.

## 2 Theoretical Background

### 2.1 Introduction to the $\mu$ SR experiment

The muon  $\mu^-$  is a spin- $\frac{1}{2}$  particle (fermion), has a charge of  $-e$  and a mass of  $m_\mu \approx 1.88 \times 10^{-25}$  g [12], which is about 207 times the electron mass  $m_e$  [1]. It is therefore often regarded as a heavy electron, while its anti-particle, the anti-muon  $\mu^+$ , which has the same mass and a charge of  $+e$ , can be considered as a light proton due to the positive charge and the mass ratio  $\frac{m_\mu}{m_p} \approx \frac{1}{9}$  [1].  $\mu$ SR originates from particle physics, but has since evolved into a local probe technique with a wide range of applications like examining superconductors or magnetic materials. In  $\mu$ SR, the time evolution of the muon spin is measured, which provides information on its local magnetic environment. Typically, anti-muons are utilized due to the increased production rates and maintained polarization during sample implantation compared

to negative muons [2]. The virtually complete spin polarization of the anti-muons is a direct result of their production. First, positive pions  $\pi^+$  are produced by colliding protons  $p$  with a carbon target using a particle accelerator, which, among other things, gives rise to pions via the process



where  $n$  represents a neutron. The generated pions have a spin of 0 and a mean lifetime  $\tau_{\pi^+} \approx 26$  ns [12]. They then decay almost exclusively to anti-muons ( $\tau_{\mu^+} \approx 2.2$   $\mu$ s [12]) and muon-neutrinos  $\nu_\mu$ , which are both spin- $\frac{1}{2}$  particles, via the weak process



The weak force only couples left-chiral particles and right-chiral anti-particles, so it violates parity maximally. The corresponding observable to the chirality is the helicity  $h$ , which is the normalized projection of the spin  $\mathbf{s}$  onto the momentum  $\mathbf{p}$

$$h = \frac{\mathbf{s} \cdot \mathbf{p}}{|\mathbf{s}| \cdot |\mathbf{p}|} . \quad (3)$$

It can take the values  $h = \pm 1$ , which are referred to as right-handed for  $h = 1$  and left-handed for  $h = -1$ . The chirality and helicity are the same for massless particles, while the chirality is a superposition of the helicity states for massive particles. The larger the mass of a particle, the larger the admixture of the opposite-handed helicity component to a given chirality state.

When applied to the pion decay in its rest frame (Fig. 2), the nearly massless muon-neutrino ( $m_{\nu_\mu} < 1.43 \times 10^{-33}$  g [12]) must be in the  $h = -1$  state, as only its left-chiral state couples to the weak force and it has no admixture of the  $h = 1$  state. The anti-muon is forced into the same  $h = -1$  state because its momentum and spin must be opposite to the muon-neutrino due to conservation of linear and angular momenta. This is only possible because its right-chiral state is a superposition of the two helicity states due to its relatively large mass. [13]

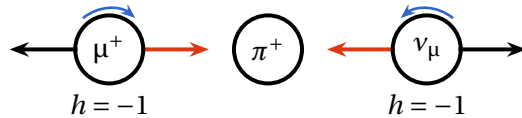


**Fig. 2:** Schematic depiction of the pion decay in the pion's rest frame, resulting in muons with defined helicity  $h = -1$ . Momenta are indicated in black, the spins in orange and chiralities in blue. The relatively large mass of the anti-muon adds admixture of the  $h = -1$  state to the right-chiral state, making the decay possible.

For convenience, the "anti-" prefix of the anti-muon will be dropped from here on, as only anti-muons are relevant for the rest of the work.

### 2.1.1 Comparison to other Magnetic Resonance Techniques

The 100% polarization of the muons is in contrast to more traditional magnetic resonance methods like nuclear magnetic resonance (NMR) and EPR, where spin-polarization is typically achieved by an externally applied magnetic field, leading to a population difference among the spin states [14]. Therefore,  $\mu$ SR has the advantage that the signal intensity is independent of the external magnetic field strength, allowing for straight-forward zero-field (ZF) measurements.

Another big difference to NMR and EPR is the detection method. In  $\mu$ SR, only one muon is implanted into the sample at a time and the positron  $e^+$  emitted during its decay

$$\mu^+ = e^+ + \nu_e + \bar{\nu}_\mu \quad (4)$$

is measured. Due to the parity violation of the weak force, the positron is preferably emitted in the direction of the muon spin. The decay anisotropy is governed by

$$W(E, \varphi) = 1 + a(E) \cos \varphi \quad (5)$$

with  $a(E)$  being the asymmetry factor and  $\varphi$  the angle between the muon spin and the emission direction of the positron [15]. The asymmetry depends on the energy of the emitted positron (Fig. 3). High-energy positrons are emitted with maximum anisotropy (blue), while low-energy positrons show isotropic emission (pink). Integration over all positron energies yields an asymmetry factor of  $a_0 = \frac{1}{3}$  (black). The asymmetry is used to reconstruct the muon spin direction during its decay, giving the time-evolution of the muon spin-polarization  $P(t)$ , if many muons are measured successively.

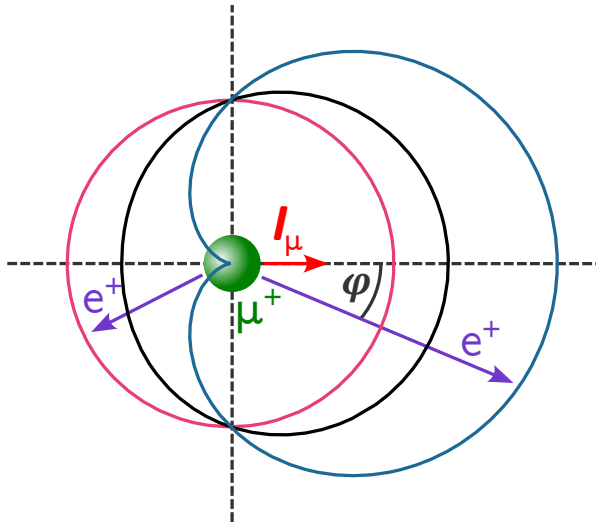


**Fig. 3:** The muon decay is anisotropic and the positron  $e^+$  is emitted preferably in the direction of the muon spin. The anisotropy depends on the energy of the emitted positron, with high-energy positrons showing maximum anisotropy (blue), while low-energy positrons are emitted isotropically (pink). Integration over all positron energies yields a decay asymmetry of  $a_0 = \frac{1}{3}$  (black), which is equivalent to the empirical maximum polarization.

In contrast to  $\mu$ SR, NMR and EPR measure the total transversal magnetic moment of the system. The reason why one measures spins of nuclei and the other of electrons is the vastly different resonance frequencies of the two, meaning that no electron spins are excited in NMR and therefore do not contribute to the signal.

### 2.1.2 Measurement Setup

The geometry of the setup is defined by whether the muon spin  $\mathbf{I}_\mu$  is oriented longitudinally (LF) or transversely (TF) to the external static magnetic field  $B_0$ . The orientation of the muon spin can be adjusted using spin rotators. A spin rotator, typically a Wien filter, works by applying mutually perpendicular electric ( $E$ ) and magnetic ( $B$ ) fields across the muon beam path. The electric field is tuned to compensate the Lorentz force generated by the magnetic field, allowing the muon's momentum  $\mathbf{p}_\mu$  to remain undeflected while its spin precesses to the desired orientation. A schematic overview of a TF setup is given in Fig. 4, while the setup used for the LF experiments is shown later in Section 3.1.

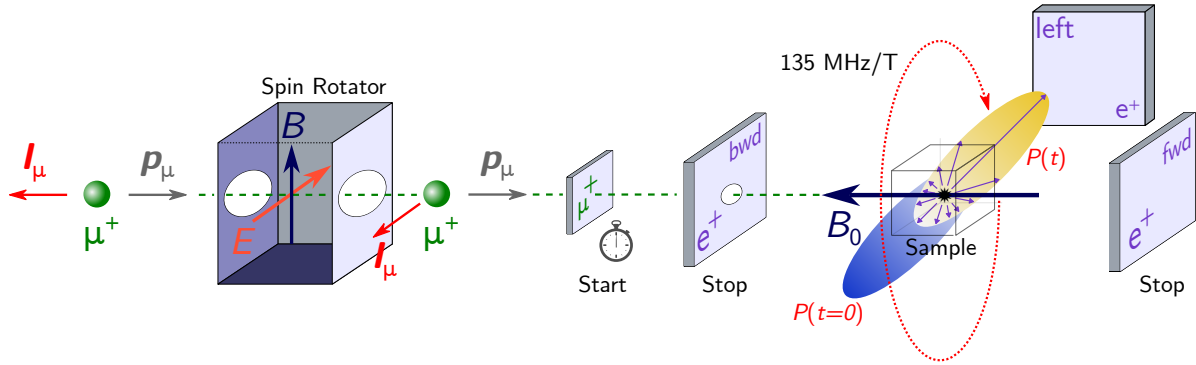


**Fig. 4:** Schematic overview of a TF- $\mu$ SR setup. First, the muon spin  $\mathbf{I}_\mu$  is rotated using a spin rotator to be transverse to the muon momentum  $\mathbf{p}_\mu$ . The muon then passes a muon detector which starts the data acquisition. The muon then enters the sample with its spin precessing around the static magnetic field  $B_0$ . The left and right (or up and down) positron detectors are used for data collection. The right detector is not depicted for simplicity.

The asymmetry of the positron emission is determined by employing two opposite facing detectors. Their summed positron count time-evolution  $N_F(t)$  and  $N_B(t)$  can then be used to determine the polarization time-evolution using

$$a_0 P(t) = \frac{N_F(t) - \alpha N_B(t)}{N_F(t) + \alpha N_B(t)} \quad (6)$$

with  $\alpha$  being a calibration constant for the spectrometer (see Fig. 5) [2]. The noise in the asymmetry increases with larger time  $t$  due to both  $N_F(t)$  and  $N_B(t)$  converging towards zero.

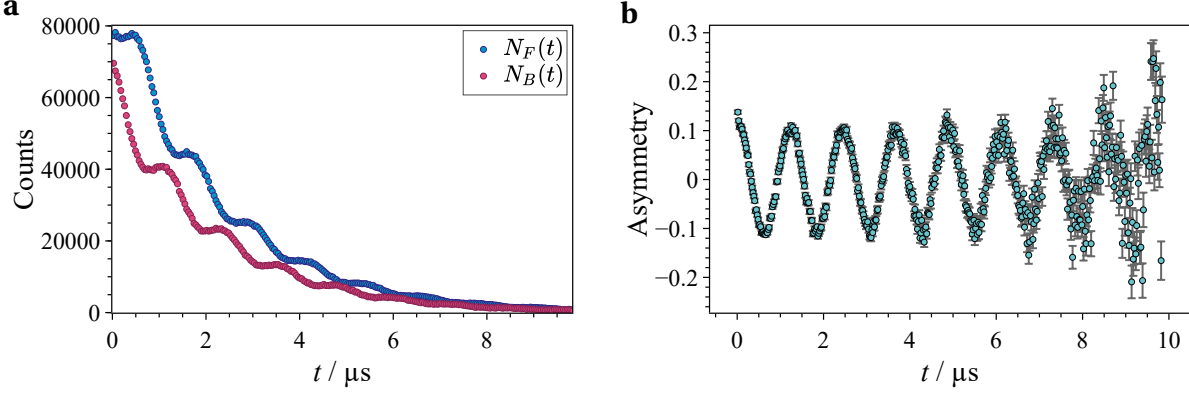


**Fig. 5:** Measured time-evolution of the positron count (**a**), from which the decay asymmetry (**b**) can be calculated using Eq. 6. The noise in the asymmetry increases drastically at large times  $t$ . The measurement was conducted on S-1, with an external field of 6 mT at 260 K.

## 2.2 Muonium

In the cases relevant to this work, the muons implanted into a solid can bind with an electron, forming coupled electron-muon centers, i.e. Mu [8]. The spin Hamiltonian of Mu is given by two Zeeman terms and the hyperfine interaction, namely

$$\hat{\mathcal{H}}/\hbar = \omega_S \hat{S}_z + \omega_I \hat{I}_z + \hat{\mathbf{S}}^T \mathbf{A} \hat{\mathbf{I}} \quad (7)$$

with  $\omega_S = \gamma_S B_0$  and  $\omega_I = -\gamma_I B_0$  being the electron and muon Larmor frequencies.  $\hat{\mathbf{S}}$  and  $\hat{\mathbf{I}}$  are the vectors of spin operators  $\hat{\mathbf{S}} = (\hat{S}_x, \hat{S}_y, \hat{S}_z)^T$  and  $\hat{\mathbf{I}} = (\hat{I}_x, \hat{I}_y, \hat{I}_z)^T$ , respectively. The Hamiltonian is analogous to two spin- $\frac{1}{2}$  systems found in EPR and NMR spectroscopy [9, 16].

The hyperfine interaction can further be split into an isotropic and anisotropic part via

$$\mathbf{A} = A_{\text{iso}} \cdot \mathbb{1} + \mathbf{T} \quad (8)$$

where  $A_{\text{iso}}$  is the isotropic coupling constant and  $\mathbf{T}$  the dipolar coupling tensor. The dipolar coupling tensor needs to be traceless, as it would otherwise lead to the existence of magnetic monopoles, yielding

$$\mathbf{T} = \begin{pmatrix} -D_{\parallel}/2 & 0 & 0 \\ 0 & -D_{\parallel}/2 & 0 \\ 0 & 0 & D_{\parallel} \end{pmatrix} \quad (9)$$

in the hyperfine principal axes system (PAS), with  $D_{\parallel}$  being the dipolar coupling constant [9, 14]. The axial symmetry results from the symmetry of the spin-only dipole-dipole interaction and can be derived directly from its Hamiltonian

$$\hat{\mathcal{H}}_{\text{DD}}/\hbar = \frac{1}{2} D_{\parallel} (3(\hat{\mathbf{S}} \cdot \mathbf{e})(\hat{\mathbf{I}} \cdot \mathbf{e}) - \hat{\mathbf{S}} \cdot \hat{\mathbf{I}}) \quad (10)$$

for two spins  $S$  and  $I$ , where  $\mathbf{e}$  is the unit vector parallel to the distance vector of the two spins [16]. The axial symmetry is obtained by using the PAS of the dipole interaction, where  $\mathbf{e} = (0, 0, 1)^T$ , yielding

$$\hat{\mathcal{H}}_{DD}/\hbar = \frac{1}{2} D_{\parallel} (3(\hat{S}_z \hat{I}_z) - \hat{\mathbf{S}} \cdot \hat{\mathbf{I}}) = \frac{1}{2} D_{\parallel} (2\hat{S}_z \hat{I}_z - \hat{S}_x \hat{I}_x - \hat{S}_y \hat{I}_y) = \hat{\mathbf{S}}^T \mathbf{T} \hat{\mathbf{I}} . \quad (11)$$

In the point-dipole approximation, which is valid for Mu,  $D_{\parallel}$  is given by

$$D_{\parallel} = 2 \frac{\hbar \mu_0}{4\pi} \frac{\gamma_e \gamma_\mu}{R_M^3} \approx \frac{503 \text{ MHz} \cdot \text{\AA}^3}{R_M^3} \quad (12)$$

where  $R_M^3$  is the distance between the muon and electron. The value of  $D_{\parallel}$  only depends on  $R_M^{-3}$ , as the rest are constants. For  $R_M = 1 \text{ \AA}$ ,  $D_{\parallel} = 503 \text{ MHz}$ , while doubling  $R_M$  to  $2 \text{ \AA}$  already reduces  $D_{\parallel}$  to  $D_{\parallel} \approx 63 \text{ MHz}$ .

### 2.2.1 Strong and Weak Coupling Limit

Different terms dominate the Hamiltonian given in Eq. 7 depending on the strength of the external static magnetic field. At large magnetic fields, where the weak coupling limit  $|A_{\text{isol}}|, |D_{\parallel}| \ll |\omega_S - \omega_I|$  holds, the Zeeman terms outweigh the hyperfine interaction. In that case the projections of the electron and muon spins onto the magnetic field axis,  $m_S$  and  $m_I$ , are good quantum numbers and the Zeeman basis  $|S, m_S, I, m_I\rangle$  can be used to describe the different spin states. The eigenstates of Mu are  $|1\rangle = |\alpha\alpha\rangle$ ,  $|2\rangle = |\alpha\beta\rangle$ ,  $|3\rangle = |\beta\alpha\rangle$  and  $|4\rangle = |\beta\beta\rangle$ , with  $|\alpha\rangle = |\frac{1}{2}, \frac{1}{2}\rangle$  and  $|\beta\rangle = |\frac{1}{2}, -\frac{1}{2}\rangle$ . In the low-field limit  $|A_{\text{isol}}|, |D_{\parallel}| \gg |\omega_S - \omega_I|$ , the hyperfine term becomes non-negligible leading to the mixing of states  $|2\rangle$  and  $|3\rangle$  due to the off-diagonal elements introduced by the hyperfine coupling tensor. The physical reason for the state mixing is that  $m_S$  and  $m_I$  are no longer good quantum numbers and the projection  $m_J$  of the total spin  $J = S + I$  has to be used. The new basis is given by  $|J, m_J\rangle$ , which can be represented in the Zeeman basis via  $|1\rangle = |1, 1\rangle = |\alpha\alpha\rangle$ ,  $|2\rangle = |1, 0\rangle = \frac{1}{\sqrt{2}}(|\alpha\beta\rangle + |\beta\alpha\rangle)$ ,  $|4\rangle = |1, -1\rangle = |\beta\beta\rangle$  and  $|3\rangle = |0, 0\rangle = \frac{1}{\sqrt{2}}(|\alpha\beta\rangle - |\beta\alpha\rangle)$ . The two coupling regimes are depicted in Fig. 6 together with a Breit-Rabi diagram showing the energy levels of Mu with purely isotropic hyperfine coupling, i.e.  $A_{\text{iso}} \neq 0 = D_{\parallel}$ . It is apparent from the curvature of the Breit-Rabi diagram that, for low magnetic field strengths, Mu cannot be described in the Zeeman basis anymore.

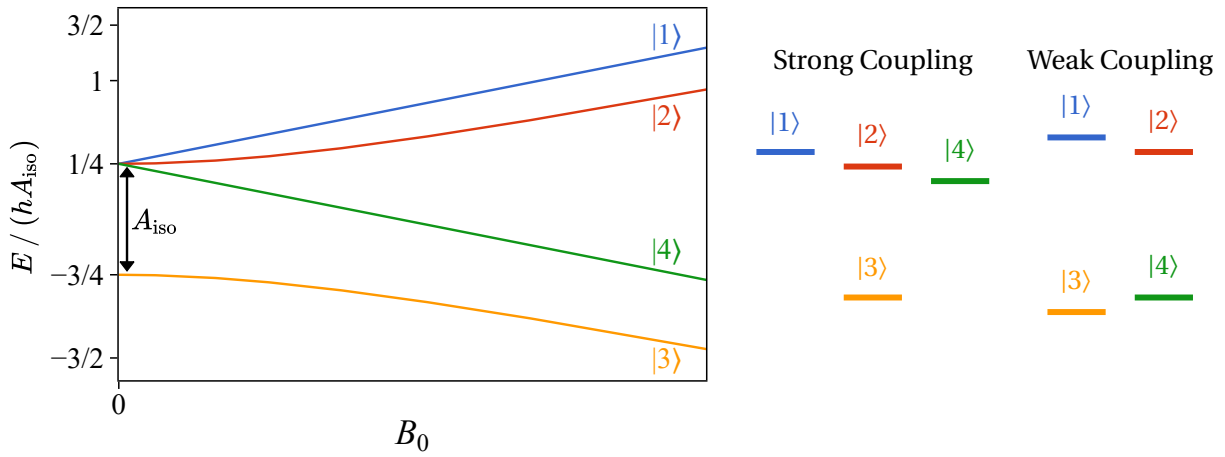


**Fig. 6:** Breit-Rabi diagram of Mu with purely isotropic coupling ( $A_{\text{iso}} \neq 0 = D_{\parallel}$ ) and schematic energy-level diagrams for the strong and weak coupling limits (not to scale). At ZF, in the strong-coupling limit, the states are given by the coupled basis  $|J, m_J\rangle$ . The triplet ( $J = 1$ ) and singlet ( $J = 0$ ) states are split by  $A_{\text{iso}}$ . At small  $B_0$  the triplet states start splitting up. For large  $B_0$ , much larger than shown, the spins are weakly coupled and are best described in the Zeeman basis  $|S, m_S, I, m_I\rangle$ .

At ZF, all Zeeman terms become zero. Therefore, splitting of the energy levels is governed only by the hyperfine interaction. The spins are strongly coupled with the three triplet states  $|1\rangle$ ,  $|2\rangle$  and  $|4\rangle$  being degenerate, while the singlet state  $|3\rangle$  is shifted to lower energy by  $A_{\text{iso}}$ . The ZF energy levels change for only anisotropically coupled Mu, i.e.  $D_{\parallel} \neq 0 = A_{\text{iso}}$ . The 4 states split into three distinct levels instead of two because one of the triplet states is lowered in energy. The singlet state is raised by the same amount, so the total energy remains the same. Which triplet state is shifted depends on the angle  $\theta$  between the interspin vector and the applied magnetic field. Breit-Rabi diagrams for  $\theta = 0^\circ$  and  $\theta = 45^\circ$  are shown in Figs. 7a and 7b, respectively.

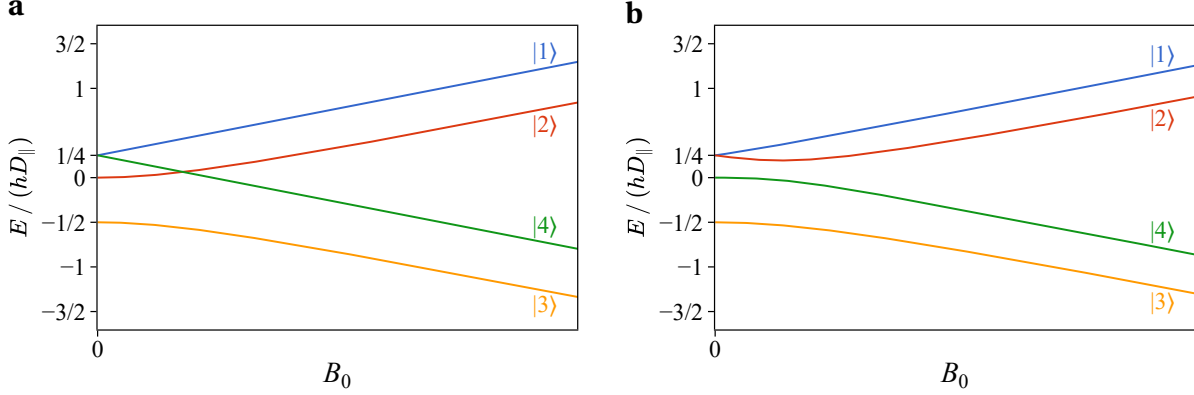


**Fig. 7:** Breit-Rabi diagram of Mu with purely anisotropic coupling ( $D_{\parallel} \neq 0 = A_{\text{iso}}$ ) for  $\theta = 0^\circ$  **(a)** and  $\theta = 45^\circ$  **(b)**.  $\theta$  mainly has an influence on the ZF state ordering and the low-field limit, while only leading to a small energy shift in the high-field limit. A true level-crossing of  $|2\rangle$  and  $|4\rangle$  is obtained for  $\theta = 0$ , whereas an avoided crossing results for  $\theta = 45^\circ$ .

### 2.2.2 Zero-field Spectra

ZF spectra can be simulated to study the system's behavior in the low-field limit. For the same system, different ZF spectra arise for  $\mu$ SR compared to NMR and EPR, due to the differing detection operators. They are given by  $\hat{O}_{\mu\text{SR}} = \hat{I}^+$  and  $\hat{O}_{\text{NMR}} = \hat{O}_{\text{EPR}} = \hat{S}^+ + \hat{I}^+$ , respectively. Only single-quantum (SQ) transitions are allowed, so neither the double-quantum  $|1\rangle \rightarrow |4\rangle$  nor the zero-quantum  $|2\rangle \rightarrow |3\rangle$  transitions are observed in any of the methods, unless there is state mixing. It is important to note that  $\mu$ SR experiments have a different initial state  $|\psi_i\rangle$  than NMR and EPR because of the 100% muon polarization at  $t = 0$ . The initial states in NMR and EPR spectroscopy can be described mathematically by  $|\psi_i^{\text{NMR}}\rangle = \hat{I}_z$  and  $|\psi_i^{\text{EPR}}\rangle = -\hat{S}_z$  as the spins align along  $B_0$ . Physically, however, the polarization is small and only a fraction of all nuclei/electrons contribute to the observable. For  $\mu$ SR, the initial state depends on whether TF ( $|\psi_i^{\mu\text{SR}}\rangle = \pm \hat{I}_x$ ) or LF ( $|\psi_i^{\mu\text{SR}}\rangle = \pm \hat{I}_z$ ) measurements are taken, both featuring virtually 100% muon spin polarization. The initial state is set using spin rotators with the sign depending on the relative orientation to  $B_0$ . For the simulated ZF spectra, the initial states were assumed to be  $|\psi_i^{\mu\text{SR}}\rangle = |\psi_i^{\text{NMR}}\rangle = \pm \hat{I}_x$  and  $|\psi_i^{\text{EPR}}\rangle = \pm \hat{S}_x$ , which are the states for TF- $\mu$ SR and NMR/EPR measurements after a  $\pi/2$  pulse.

While NMR and EPR only allow observing the  $|1\rangle \rightarrow |2\rangle$  and  $|2\rangle \rightarrow |4\rangle$  transitions, all allowed transitions are visible in  $\mu$ SR spectra (see Figs. 8 and 9). This results in fundamentally different spectra for the two typical edge cases, where either  $A_{\text{iso}}$  or  $D_{\parallel}$  is set to zero, while the effect of the other coupling is observed. Note that the ZF NMR spectra are identical to the homonuclear strong coupling spectra commonly found in NMR textbooks [16].

Moreover, the time evolution of a quantum system is given by the Liouville-von Neumann equation

$$\frac{d\hat{\sigma}}{dt} = [\hat{H}, \hat{\sigma}] \quad (13)$$

which results in systems where  $[\hat{H}, \hat{\sigma}] = 0$  being constant over time. This leads to the zero-frequencies observed in the spectra for purely isotropically coupled Mu (Fig. 8b). In NMR and EPR, the total angular

momentum  $J$  is measured with  $m_J$  being a good quantum number at ZF. Consequently, the system must be in an eigenstate of the Hamiltonian, resulting in the commutator being  $[\hat{H}, \hat{\sigma}] = 0$ . For the angular momentum  $I$  of the muon, on the contrary,  $m_I$  is not a good quantum number, but still has some time-constant component, which leads to the zero-frequency component seen in the TF- $\mu$ SR spectrum.

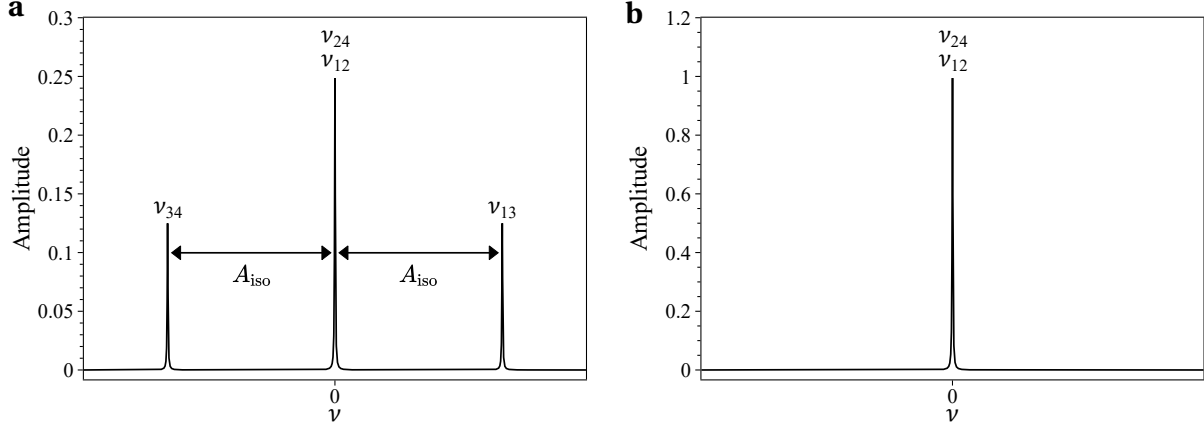


**Fig. 8:** Schematic ZF  $\mu$ SR (a) and NMR/EPR (b) spectra for Mu with purely isotropic coupling of  $A_{\text{iso}} = 2$  MHz. The different detection operators, namely  $\hat{O}_{\mu\text{SR}} = \hat{I}^+$  and  $\hat{O}_{\text{NMR}} = \hat{O}_{\text{EPR}} = \hat{S}^+ + \hat{I}^+$ , lead to contrasting spectra. The  $\mu$ SR spectrum displays three peaks split by  $A_{\text{iso}}$ , where the two outer ones are SQ transitions and the middle is the sum of both SQ muon transitions. Only the muon transitions are observed in the NMR/EPR spectrum, giving rise to a singular peak.

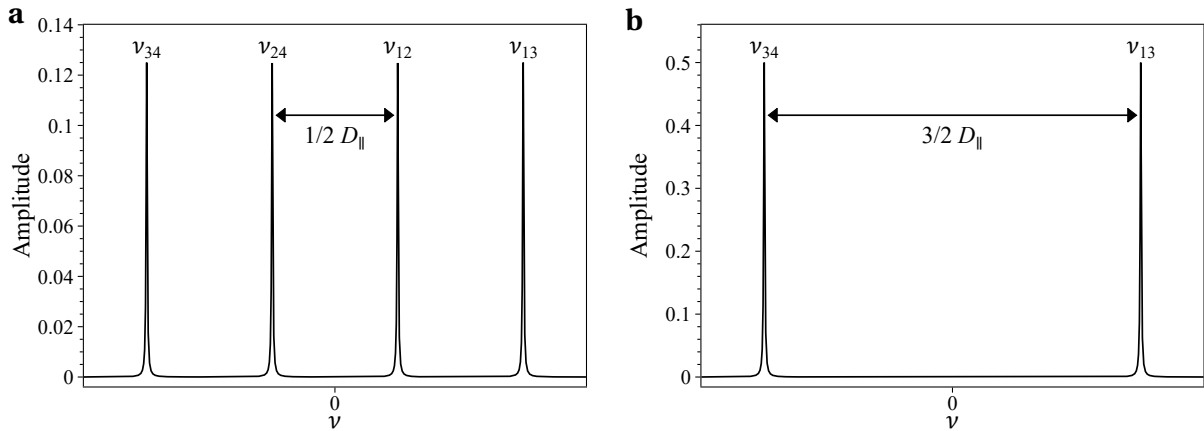


**Fig. 9:** Same ZF spectra as in Fig. 8, but with only the anisotropic coupling of  $D_{\parallel} = 2$  MHz. The two outer peaks in the  $\mu$ SR spectrum are SQ muon transitions, while the inner peaks are SQ electron transitions. In the NMR spectrum, only the muon transitions are observed.

Note that less transitions are observed in the NMR spectra but the sum of the peak intensities is 1 compared to the  $\frac{1}{2}$  for the  $\mu$ SR spectra. This is a result of the norm of the utilized detection operators.

### 2.2.3 Repolarization

One possibility to determine  $A_{\text{iso}}$  experimentally is by using LF repolarization.  $B_0$  is applied parallel to the muon spin and the initial muon polarization of Mu is measured as a function of  $B_0$  [14]. At  $B_0 \rightarrow 0$ , before the formation in Mu, the muon is polarized while the electron is not. During Mu formation, spin state mixing transfers muon polarization to the electron. This mixing is largest when the Zeeman terms are zero and smallest, when the Zeeman interaction outweighs the hyperfine coupling.

Experimentally  $A_{\text{iso}}$  is determined by fitting the measured muon polarization as a function of  $B_0$  to the theoretical expression

$$P_z(B_0) = \frac{1 + 2 \left( \frac{B_0}{B_{75}} \right)^2}{2 \left\{ 1 + \left( \frac{B_0}{B_{75}} \right)^2 \right\}} \quad (14)$$

where  $B_{75} = \frac{A_{\text{iso}}}{\gamma_e + \gamma_\mu}$  [17]. Generally, repolarization measurements are inferior to other methods, like avoided level-crossings (ALC) and TF experiments, for determining  $A_{\text{iso}}$ , due to their lower accuracy. However, it is still used as it is relatively easy to measure and it can be used to determine the fraction of muons that form Mu after implantation into the sample.

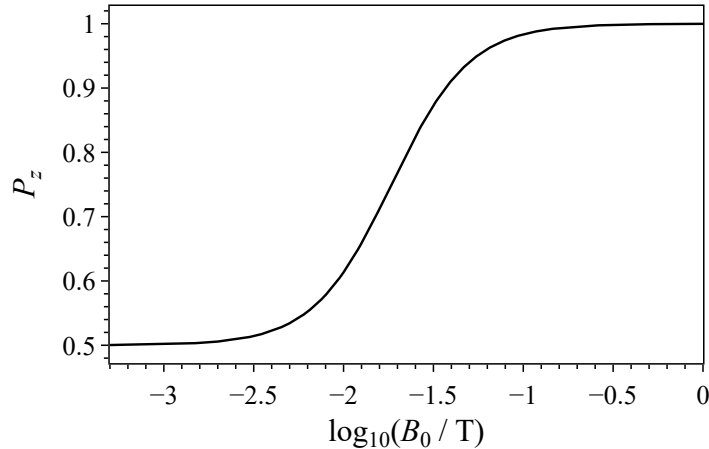


**Fig. 10:** Muon polarization at different  $B_0$  after forming Mu with  $A_{\text{iso}} = 514.8$  MHz. The muon polarization increases drastically at larger magnetic field strengths and is nearly fully recovered at  $B_0 = 0.1$  T.

### 2.2.4 Avoided Level-Crossing Resonance

The energy-levels of the different spin states can undergo avoided level-crossings (ALCs), as the dependence on the external magnetic field  $B_0$  is not equal for all spin states (Fig. 11). Therefore, measurements of the time-integrated asymmetry of the muon decay as a function of  $B_0$  can lead to the observation of resonances. The resonances are denoted as  $\Delta_{\Delta M}$ , where  $\Delta M$  indicates the change in the sum of the  $m_z$  quantum numbers of the particles in the system, i.e. the electron and muon for Mu. The theory for ALC resonances was developed for three spin systems consisting of an electron, muon and nucleus. In such

systems,  $\Delta M = 2$  (muon-proton flip-flip) as well as  $\Delta M = 0$  (muon-proton flip-flop) resonances can be observed [14]. This work focuses on electron-muon systems, where only  $\Delta M = 1$  related to muon flips are seen. In these systems, ALCs can only occur in Mu with  $D_{\parallel} \neq 0$ , which leads to state mixing at level-crossings. In contrast, true crossings are observed for Mu with purely isotropic hyperfine coupling, since there are no off-diagonal terms that couple the levels that cross.

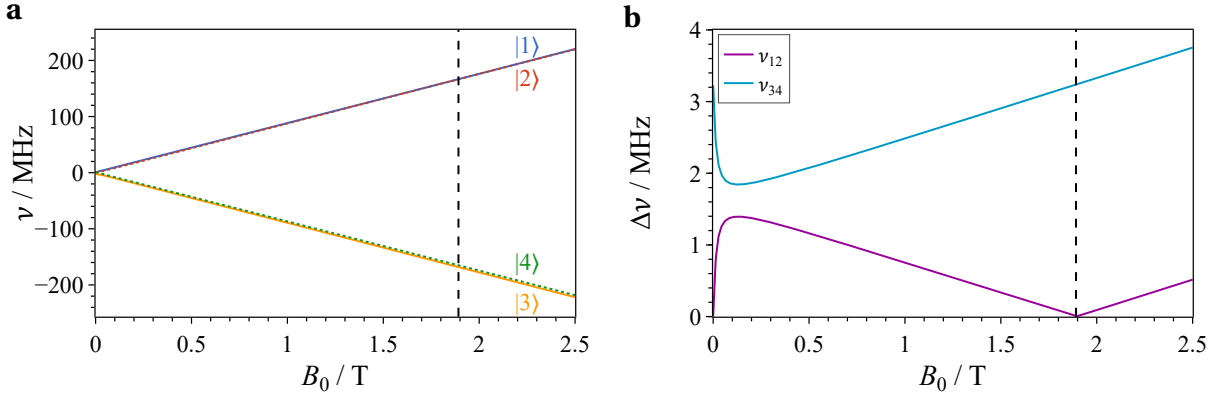


**Fig. 11:** Numerically simulated Breit-Rabi Diagram for Mu with  $A_{\text{iso}} = 514.8$  MHz and  $D_{\parallel} = 2$  MHz (a) and the transition frequency between the upper two ( $v_{12}$ ) and lower two states ( $v_{34}$ ) (b). The upper two states cross at  $B = 1.8922$  T (black, dashed line), giving rise to a  $\Delta_1$  resonance.

An analytical expression has been derived for axially symmetric hyperfine tensors to describe the dependence of the muon polarization  $P_z$  on  $B_0$  and  $\theta$  [18]. The expression is given by

$$P_z(B, \theta) = 1 - \frac{0.5q^2 P_z^0}{(\lambda/2\pi)^2 + q^2 + (v_{\mu} - v_{\mu}^0)^2} \quad (15)$$

where  $q$  and  $v_{\mu}^0$  are further defined as

$$q = \frac{3}{4} D_{\parallel} \sin \theta \cos \theta \quad (16)$$

and

$$v_{\mu}^0 = \frac{1}{2} \left[ A_{\text{iso}} + \frac{D_{\parallel}}{2} (3 \cos^2 \theta - 1) \right] . \quad (17)$$

The relaxation rate  $\lambda = \lambda_0 + \lambda'$  depends on the inverse muon lifetime  $\lambda_0 = 0.4551 \mu\text{s}^{-1}$  and  $\lambda'$ , which is the rate of (chemical) transformation to a state off resonance. Electron flips, which are governed by  $T_1^{e^-}$ , also add to the relaxation rate [19]. Numerical integration over  $\theta$  with  $\sin \theta$ -weighting yields the powder spectrum, which is displayed in Fig. 12. A comparison of the analytical spectra to numerical simulations can be found in Section 4.1. The hyperfine constants can be determined by fitting experimental spectra to either the analytical expression or numerically calculated spectra.

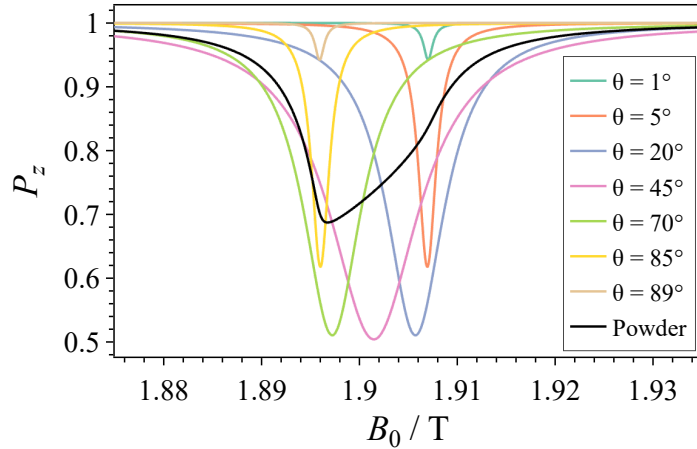


**Fig. 12:** Theoretical ALC powder spectrum together with selected single-crystal spectra for  $A_{\text{iso}} = 514.8 \text{ MHz}$  and  $D_{\parallel} = 2 \text{ MHz}$ . The  $\sin\theta$ -weighting causes the powder spectrum to be asymmetric.

In ALC- $\mu$ SR, each measured time trace is integrated, with each trace yielding one data point in the spectrum. Peaks appear as dips because on-resonant time traces show oscillations with greater amplitude but lower frequency compared to off-resonant counterparts (Fig. 13). Therefore, integration over on-resonant time traces results in lower a  $P_z$  compared to off-resonant traces.

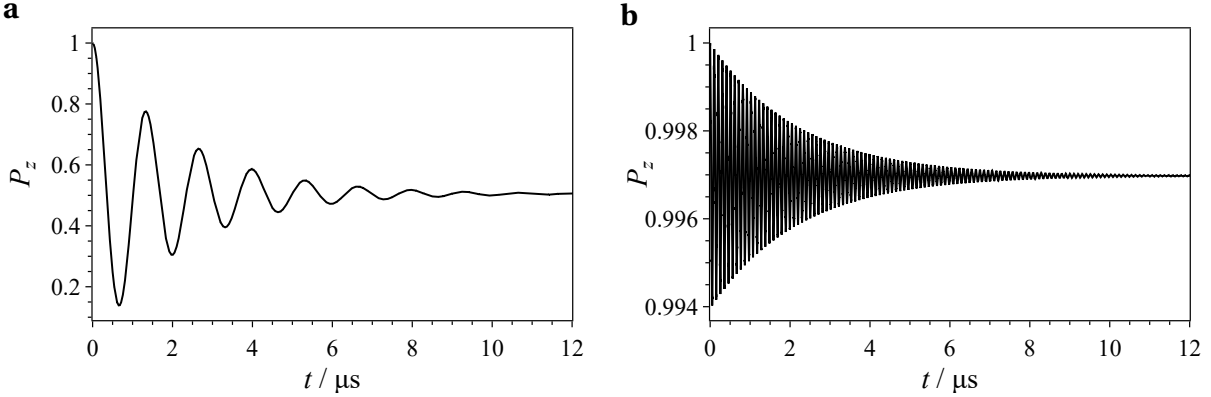


**Fig. 13:** Simulated ALC- $\mu$ SR time traces with for on- and off-resonant  $B_0$ , displayed in (a) and (b), respectively. The simulations are based on the same system as Fig. 12. Both traces were simulated using  $\theta = 45^\circ$ , using  $B_0 = 1.8922 \text{ T}$  for the on-resonant case and  $B_0 = 1.8200 \text{ T}$  for the off-resonant case. The muon decay was introduced phenomenologically by setting  $T_1 = T_2 = 2.2 \mu\text{s}$ . The on-resonance case results in a slower oscillation but larger amplitude, while for the off-resonance trace the polarization oscillates with a higher frequency but remains close to 1. Integrating a time trace yields one data point in a single-orientation ALC spectrum.

### 2.2.5 Multi-Quantum Approach

The Hamiltonian given in Eq. 7 can be simplified for weakly, anisotropically coupled Mu by applying the high-field approximation for the electron. Defining  $A = A_{zz}$  and  $B = \sqrt{A_{zx}^2 + A_{zy}^2}$  yields the truncated

Hamiltonian

$$\hat{\mathcal{H}}_{\text{trunc.}}/\hbar = \omega_S \hat{S}_z + \omega_I \hat{I}_z + A \hat{S}_z \hat{I}_z + B \hat{S}_z \hat{I}_x. \quad (18)$$

The pseudo-secular term  $B \hat{S}_z \hat{I}_x$  makes the formally forbidden zero- and double-quantum transitions with  $|\Delta m_S| = |\Delta m_I| = 1$  partially allowed. This is best understood by looking at the local fields at the muon position in a semi-classical magnetization vector picture (Fig. 14). The quantization axis of the muon is distinct for the different electron spin states, leading to tilts of  $\eta_\alpha$  and  $\eta_\beta$ , respectively.

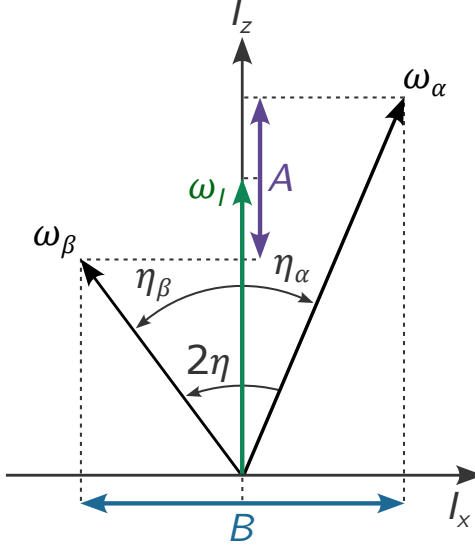


**Fig. 14:** Semi-classical magnetization vector picture showing the local fields ( $\omega = \gamma_I B_{\text{local}}$ ) at the muon position. The muon quantization axis is parallel to  $\omega_\alpha$  or  $\omega_\beta$  depending on whether the electron is in the  $|\alpha\rangle$  or  $|\beta\rangle$  state. Flipping the electron spin also changes the quantization axis of the muon, enabling  $|\Delta M| = 2$  (flip-flip) and  $|\Delta M| = 0$  (flip-flop) transitions.

It can be shown that the truncated Hamiltonian can be diagonalized by rotating the manifolds by their respective tilting angles [9]. These two transformations are independent from one another and can be combined to the unitary transformation

$$\hat{U}_{\text{EB}} = \exp \left( -i \left[ \eta_\alpha \hat{S}^\alpha \hat{I}_y - \eta_\beta \hat{S}^\beta \hat{I}_y \right] \right) = \exp \left( -i \left[ \xi \hat{I}_y + \eta 2 \hat{S}_z \hat{I}_y \right] \right) \quad (19)$$

with  $\eta = (\eta_\alpha + \eta_\beta)/2$  and  $\xi = (\eta_\alpha - \eta_\beta)/2$ . The second form has the advantage that the  $\xi \hat{I}_y$  term commutes with the electron spin operators, meaning that only the  $\eta 2 \hat{S}_z \hat{I}_y$  term is responsible for rotating them to the eigenbasis of the truncated Hamiltonian. The quantization axis tilting angles  $\eta_\alpha$  and  $\eta_\beta$  are given by

$$\eta_\alpha = \arctan \left( \frac{-B}{2\omega_I + A} \right) \quad \text{and} \quad \eta_\beta = \arctan \left( \frac{B}{2\omega_I - A} \right). \quad (20)$$

Electron spin transitions are described by  $\hat{S}_x$  in the eigenbasis of the Hamiltonian, namely

$$\hat{U}_{\text{EB}} \hat{S}_x \hat{U}_{\text{EB}}^\dagger = \cos \eta \hat{S}_x + \sin \eta 2 \hat{S}_y \hat{I}_y. \quad (21)$$

SQ transitions result from  $\hat{S}_x$ , while the zero- and double-quantum transitions are driven by  $2\hat{S}_y \hat{I}_y$ , which becomes apparent by rewriting  $2\hat{S}_y \hat{I}_y$  as

$$2\hat{S}_y \hat{I}_y = \underbrace{\hat{S}^+ \hat{I}^- + \hat{S}^- \hat{I}^+}_{\text{zero-quantum}} - \underbrace{\hat{S}^+ \hat{I}^+ - \hat{S}^- \hat{I}^-}_{\text{double-quantum}}. \quad (22)$$

As transition probabilities are given by the absolute squares of the transitions amplitude, the resulting transitions probabilities for the allowed and forbidden transitions are proportional to  $\cos^2 \eta$  and  $\sin^2 \eta$ , respectively.

Driving MQ transitions results in Rabi oscillations in the time domain signal. Their frequency is given by  $\omega_{\text{eff}} = \sqrt{\omega_1^2 + \Omega^2}$  with  $\omega_1$  being the Rabi frequency and  $\Omega = \omega_0 - \omega_{\mu\text{w}}$  describing the detuning from the resonance. This results in a lower frequency for on-resonant driving of the MQ transitions but a large amplitude. Off-resonant driving results in a higher frequency but much lower amplitude.

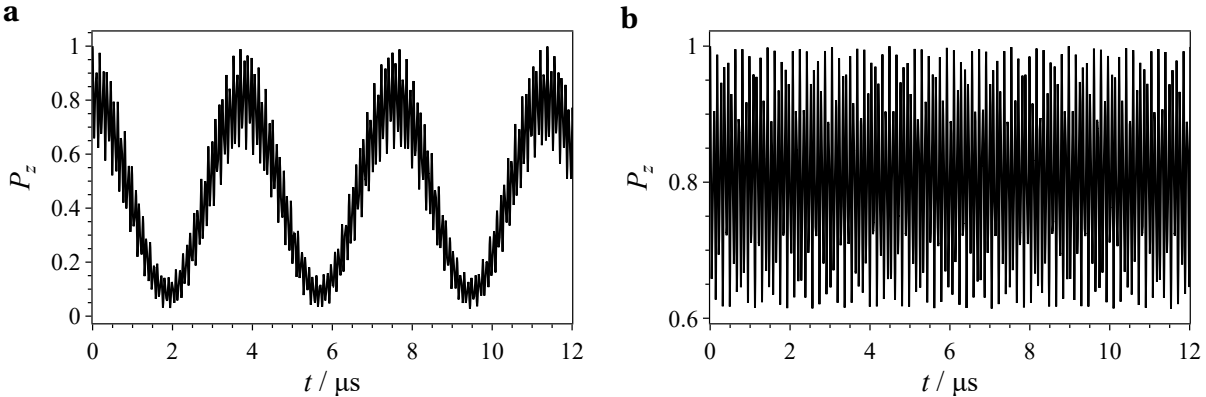


**Fig. 15:** Simulated time traces of the muon polarization during on- and off-resonant driving of a MQ transition, displayed in (a) and (b), respectively. The microwave frequency was set to  $\nu_{\mu\text{w}} = 2.3037$  GHz and the magnetic fields were swept. Both were simulated using  $\theta = 45^\circ$ ,  $A_{\text{iso}} = 3$  MHz and  $D_{\parallel} = 15.5$  MHz as parameters. Neither spin-relaxation nor the muon decay were considered. Like in the ALC simulations in Fig. 13, the on-resonance case results in a lower Rabi oscillation frequency but larger changes of the polarization, while for the off-resonance trace the polarization oscillates with a higher frequency but never goes below  $P_z = 0.6$ . Integration of one time trace yields a data point in a single-orientation MQ spectrum.

To attain the final MQ spectrum, the time traces are integrated, yielding the LF asymmetry of one data point in the spectrum. The increased amplitude of on-resonance Rabi oscillations results in a decreased LF asymmetry value. In the case of single-crystal measurements, the Rabi oscillations are resolvable if conducted at temperatures low enough for a sufficiently long transverse electron relaxation  $T_2^{\text{e}^-}$  [8]. But for powder measurements, no Rabi oscillations are observable due to the averaging over all angles and the fact that many measurements are acquired at room temperature, which leads to fast  $T_2^{\text{e}^-}$  relaxation

times. Therefore, only a decrease in the asymmetry is visible in the time domain. Fig. 16 displays experimental MQ- $\mu$ SR time traces with and without microwave excitation. Note that the microwave irradiation only starts after the dead time of  $t \approx 300$  ns, leading to a sudden decrease in  $A(t)$  (see Section 3.1 for further details). As MQ spectra are retrieved by integration over these traces, resonances result in a dip in the MQ spectrum, as seen in e.g. Fig. 1.

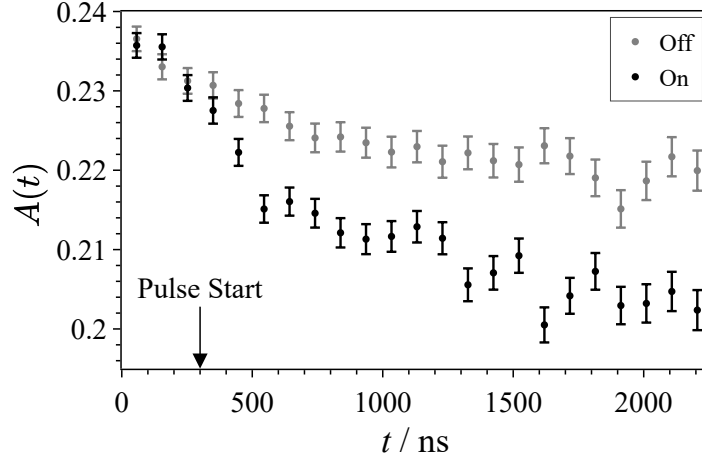


**Fig. 16:** Muon decay asymmetry  $A(t)$  in SrTiO<sub>3</sub> as a function of time with and without on-resonant microwave excitation on the electron of MQ transitions. For the trace with microwave irradiation, the pulse starts at  $t \approx 300$  ns. The excitation leads to a transfer of polarization from the muon to the electron, decreasing  $A(t)$ . The measurement was done at 17 K with an external magnetic field of  $B_0 = 118$  mT. The microwave frequency was set to  $\nu_{\mu\text{w}} = 3.335$  GHz.

## 3 Experimental

### 3.1 Setup

The MQ- $\mu$ SR experiments were conducted on the general purpose surface-muon instrument (GPS) [20] with addition of a microwave excitation setup, which is described in detail in Ref. [8]. A schematic overview of the setup is given in Fig. 17. In brief, a dedicated probe head is inserted into a helium flow cryostat, which allows continuous operation down to 2 K. A half-wave microstrip resonator design with a resonance frequency of  $\approx 4$  GHz is used to generate the microwave magnetic field  $B_1$  at the sample. A programmable delay generator combined with digital microwave phase shifters ensures that basic pulse sequences can be applied to the sample. The microwave field is applied transverse to the direction of the muon beam, while the external static magnetic field  $B_0$  is antiparallel to the direction of the muon beam. The microwave pulse is triggered by the muon detector with a dead time of  $\approx 300$  ns, since the arrival time of the muon is not known a priori. Microwave pulses can be amplified to nominal powers up to 100 W. In the results section, either a power of 50 W or a close-to-maximum power of 90 W was used. In previous experiments at temperatures of 280 K, a microwave field  $B_1$  of almost 1.0 mT was achieved at

full power [8]. Accordingly, for the experiments presented below at 260 K,  $B_1$  was on the order of 0.9 mT at 90 W and 0.7 mT at 50 W. This corresponds to drive strengths  $\nu_1$  (in the rotating frame) of 13 MHz and 10 MHz, respectively. Note, however, that these are just rough estimates and the actual  $\nu_1$  remains difficult to characterize for powder samples.

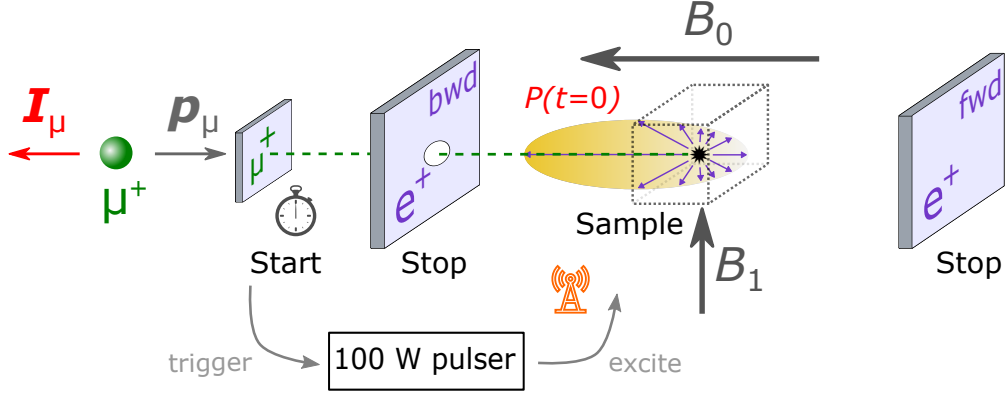


**Fig. 17:** Schematic overview of the modified GPS setup used for the MQ- $\mu$ SR experiments. A muon detector triggers the data acquisition for the positron detectors and the microwave excitation, which has a dead time of  $\approx 300$  ns. The muon enters the sample with its spin  $I_\mu$  being antiparallel to its momentum  $p_\mu$ . At the sample, the external static magnetic field  $B_0$  is applied antiparallel to the muon's momentum, while the microwave field  $B_1$  is applied in the transverse direction. The sample chamber is inside a helium flow cryostat, which allows continuous operation down to 2 K. The muon spin evolution is recorded by counting the forward (fwd) and backward (bwd) emitted positrons  $e^+$  from the muons anisotropic decay.

The ZF measurements were done on the high-field and low temperature instrument (HAL) [21]. A ZF coil allowed for passive compensation of earth's magnetic field, permitting  $B_0$  in the range of 0–1.7 mT. For cooling, a helium flow cryostat enabling cooling down to 1.6 K was used.

### 3.2 Sample Preparation

Commercially available S-1 [22] and SrTiO<sub>3</sub> [23] were used as samples. All S-1 samples were prepared under helium atmosphere and thoroughly degassed before use to minimize contamination with oxygen. After degassing, the samples were loaded quickly into the cryostats. For MQ- $\mu$ SR, the samples were sealed with kapton tape and loaded into the powder holder designed for MQ experiments. For the ZF measurements, the samples were pressed into 8.5 mm-diameter pellets.

### 3.3 Software

For the numerical simulations, the MATLAB (versions R2024a and R2025b) [24] software package Spin dynamics analysis (SPIDYAN, version 2) [25] was used, which computes the spin evolution using small time steps. A minor modification on an input parameter check was required to compute ALC spectra at

high magnetic fields on a deliberately reduced time grid, since high-frequency electron spin transitions are not excited in ALC.

The analytical simulations were done in Python (version 3.13) [26] using the QuTiP package (version 5.2.1) [27] to build the spin Hamiltonian. For the matrix diagonalization, an established matrix diagonalizer from the NumPy package (version 2.3.4) [28] was used. Consistent ordering of the eigenstates was ensured by maximizing the overlap between the new and old eigenvectors using the Hungarian algorithm [29].

ChatGPT (GPT-5 and GPT-4o) [30] and GitHub Copilot (using GPT-4.1 Copilot) [31] were used for coding assistance and code generation.

The code for the simulations, the modified version of SPIDYAN, the scripts used for data analysis and the experimental data is available on GitHub at [https://github.com/davidpwalk/MQ\\_muSR](https://github.com/davidpwalk/MQ_muSR).

## 4 Results and Discussion

### 4.1 Numerical ALC Simulations

ALC spectra retrieved by numerical spin dynamics simulations were compared to their analytical counterpart to validate the accuracy of the simulations. The hyperfine coupling constants ( $A_{\text{iso}} = 514.8$  MHz and  $D_{\parallel} = 2$  MHz [32]) of the muoniated cyclohexadienyl radical ( $\text{C}_6\text{H}_6\text{Mu}$ ) in benzene at 293 K were used, which is a commonly used benchmark system [6, 7]. The retrieved ALC powder spectra are shown in Figs. 18a and 18b together with a selection of single-crystal spectra. The simulations match the analytical spectra well, showing minor differences in peak intensities for  $\theta = 1^\circ$  and  $\theta = 89^\circ$ . Fig. 18c shows the difference in peak positions  $\Delta B_0$  of the single-crystal ALC spectra obtained via the two methods. The oscillations can be attributed to the discretization of the magnetic field in the numerical calculations, since changing the magnetic field grid resulted in different  $\Delta B_0$ . The average  $\Delta B_0$  was determined to be  $\langle \Delta B_0 \rangle = -9.2$  mT, which gives an estimate on the error of the numerical simulations. The powder spectra are compared in Fig. 18d, with the numerically calculated spectrum being shifted by  $-9$  mT for easier comparison of the line shapes. No significant difference is observed in the powder spectra. The results solidify the validity of the numerical spin dynamics simulations for exploration of the limitations of the analytical model.

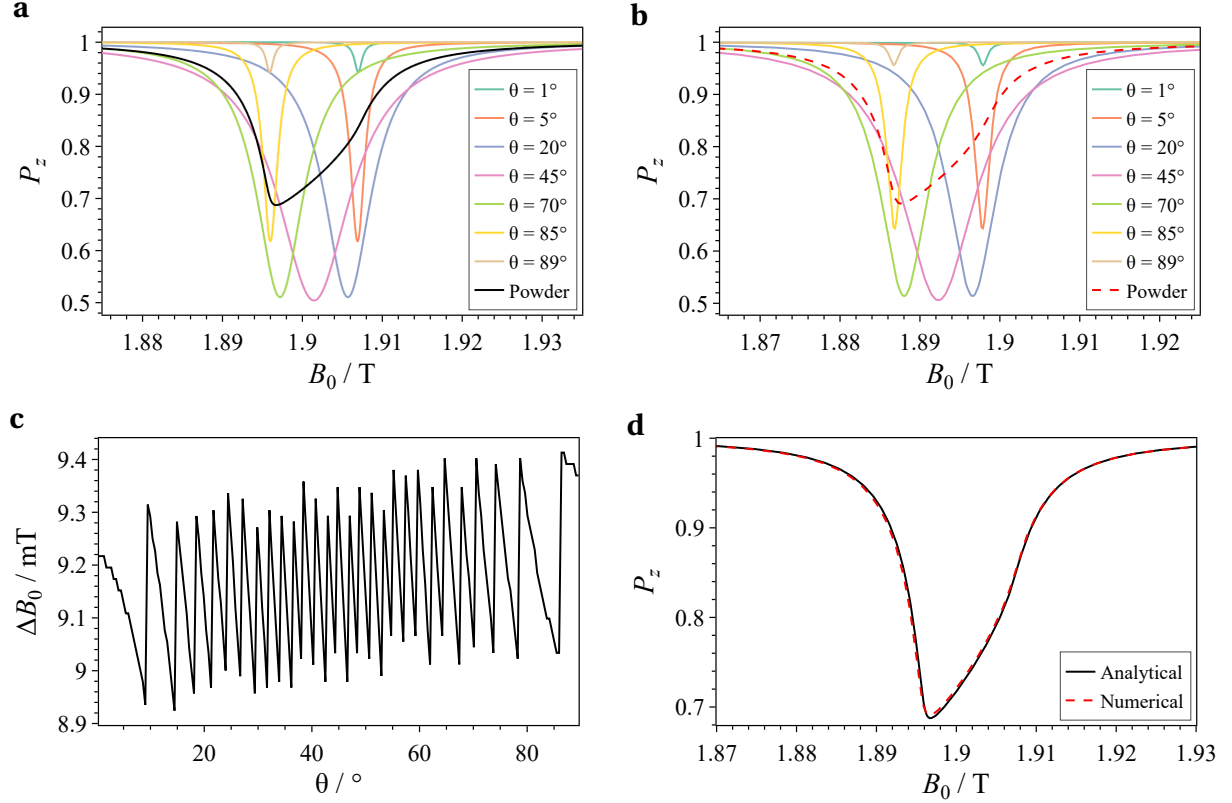


**Fig. 18:** Analytical (a) and numerically simulated (b) ALC- $\mu$ SR powder and single-crystal spectra for  $A_{\text{iso}} = 514.8$  MHz and  $D_{\parallel} = 2$  MHz. For the analytical spectra  $\lambda'$  is set to 0. The muon decay was introduced in the numerical simulations phenomenologically by setting  $T_1 = T_2 = 2.2$   $\mu$ s. The shapes and intensities of the different spectra are similar. The difference in peak position  $\Delta B_0$  of the numerical single-crystal spectra (c) and the analytical spectra oscillates around the average of  $\langle \Delta B_0 \rangle = -9.2$  mT, which gives a good estimation of the error of the numerical approach. The oscillations are caused by the discretization of the magnetic field grid in the numerical calculations. The powder spectra (d) show no significant difference when shifting the numerical spectrum by -9 mT.

## 4.2 Limit of the Analytical ALC Model

Analytical and numerical ALC spectra were calculated to test the limit of the analytical ALC model and are displayed in Fig. 19. The analytical model does not describe the muon repolarization occurring near ZF. This is to be expected as the derivation only considers ALC resonances in the high-field limit [18]. Therefore, it fails when the muon repolarization starts overlapping with the ALC resonance, which is the case for small  $A_{\text{iso}}$ , where the ALC resonance is close to zero-field. Interestingly, the peak position is not influenced by the muon repolarization as much as the intensity and shape of the peak. This results in the analytical model still being able to predict the peak positions well, even after the shape is already very different with a numerical approach.

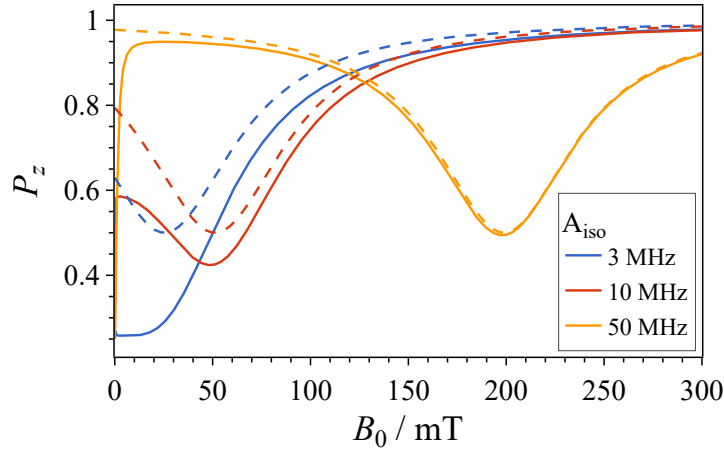


**Fig. 19:** Comparison of numerical (solid) and analytical (dashed) ALC spectra with  $\theta = 45^\circ$ ,  $D_{\parallel} = 15.5$  MHz and different  $A_{\text{iso}}$ . The muon decay was considered phenomenologically by setting  $T_1 = T_2 = 2.2$   $\mu\text{s}$ . The analytical model is incapable of describing the muon repolarization occurring at small magnetic fields. It only predicts the ALC peak position and shape with increasing accuracy, the further away the peak is from ZF. The ALC peak position shifts to larger fields with increasing  $A_{\text{iso}}$ , improving the accuracy of the analytical model. For small  $A_{\text{iso}}$ , the muon repolarization and the ALC resonance start overlapping, which can only be described by the numerical approach.

Additionally, the feasibility of ALC- $\mu$ SR to characterize weakly-coupled Mu in powder samples was assessed by computing the ALC spectrum of SrTiO<sub>3</sub> ( $A_{\text{iso}} = 1.4$  MHz,  $D_{\parallel} = 15.5$  MHz [10]). A contour plot illustrating the  $\theta$ -dependence of the ALC spectra is displayed in Fig. 20a, with Fig. 20b showing the powder spectrum together with spectra for specific  $\theta$ . The ALC resonances start shifting to lower fields with increasing  $\theta$ , overlapping with the muon repolarization. Note that muon repolarization can be viewed as an ALC at  $B_0 = 0$ . From the magic angle  $\theta \approx 54.7^\circ$  onward, the ALC resonances start shifting towards higher fields. The resulting pattern resembles a Pake pattern with the left half missing. The muon repolarization seems to distort the Pake pattern, especially around  $\theta = 45^\circ$ , where the resonance is broadened immensely. Interestingly, the spectrum reaches  $P_z = 0$  close to  $\theta = 54.7^\circ$ , which implies that the entire muon polarization oscillates. This is probably because all interactions along the z-axis vanish at this angle and at zero field. The powder spectrum's line shape makes analysis via fitting of analytical expressions unfeasible. A pronounced bend is visible at the ALC resonance position for  $\theta \rightarrow 90^\circ$  and for  $B_0 \rightarrow 0$ . Extensive numerical spin dynamics simulations would be needed to analyze the retrieved ALC powder spectra. ALC measurements are therefore deemed to be an unviable method to characterize weakly-coupled Mu.

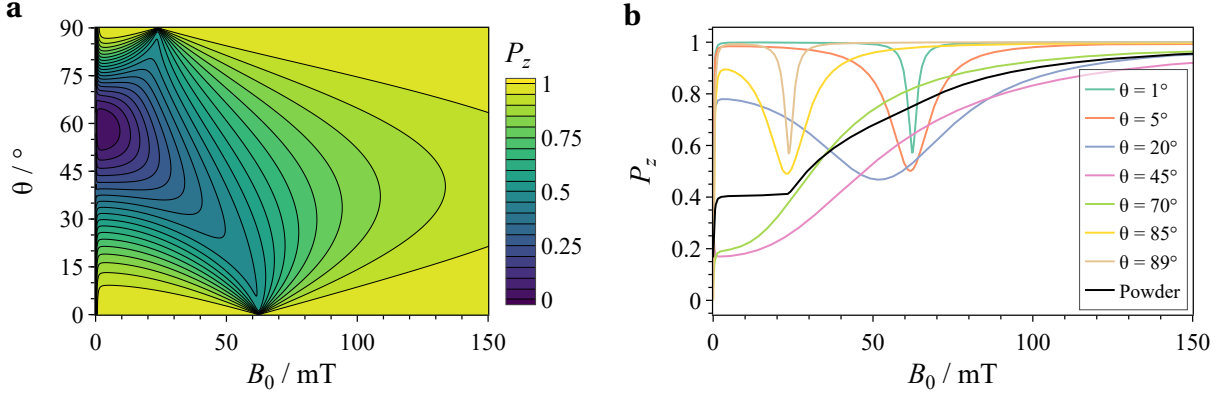


**Fig. 20:** Numerically simulated ALC- $\mu$ SR spectra of  $\text{SrTiO}_3$  ( $A_{\text{iso}} = 1.4$  MHz,  $D_{\parallel} = 15.5$  MHz [10]) for different  $\theta$ . (a) The observed pattern resembles the right half of the Pake pattern. ALC resonances close to  $B_0 = 0$  start overlapping with the muon repolarization, with broad line shapes for intermediate  $\theta$  and total state mixing, i.e. zero integrated polarization, close to the magic angle  $\theta = 54.7^\circ$ . (b) The powder spectrum shows prominent bends at the ALC resonance for  $\theta \rightarrow 90^\circ$  and the muon repolarization at  $B_0 \rightarrow 0$ . The line shape of the powder spectrum causes the analysis of ALC powder spectra of weakly-coupled Mu to be challenging. See text for more detail.

### 4.3 Parameter Dependence of Multi-Quantum Resonances

MQ transitions are exploited in many EPR techniques [9] but are mostly unused in  $\mu$ SR, with MQ- $\mu$ SR being a novel method. The influence of  $\theta$ ,  $A_{\text{iso}}$ , the electron relaxation time  $T_2^{\text{e}^-}$  and the amplitude of the microwave irradiation  $v_1$  on MQ- $\mu$ SR powder spectrum was investigated through numerical spin dynamics simulations. The simulations were performed based on the benchmark system  $\text{SrTiO}_3$ , which has been shown to form weakly-coupled Mu [10, 11]. If not specified otherwise, the following parameters were used for the simulations: The hyperfine coupling constants were set to  $A_{\text{iso}} = 1.4$  MHz and  $D_{\parallel} = 15.5$  MHz (taken from Ref. [10]). The microwave irradiation frequency was set to  $v_{\mu\text{W}} = 2.3037$  GHz with an amplitude of  $v_1 = 1$  MHz. Transverse electron spin relaxation was implemented phenomenologically by setting all relaxation times  $T_1 = T_2 = 10^9$  s, except the  $T_2$  of the electron transitions, which were defined to be  $T_2^{\text{e}^-} = 2$   $\mu$ s.

#### 4.3.1 $\theta$ -Dependence

The  $\theta$ -dependence of SQ transitions is well established and given by the Pake pattern [16]. In contrast, the  $\theta$ -dependence of MQ transitions follows a different pattern that is of importance for the MQ approach used in this work. The  $\theta$ -dependence was examined by numerically simulating the time-integrated polarization of the electron and muon. The isotropic coupling constant was set to  $A_{\text{iso}} = 0$  MHz. The initial state was set to  $P_z^{\text{e}^-} = 1$  and  $P_z^{\mu^+} = 0$  for the electron spectrum and vice versa for the muon spectrum, mimicking the conditions in EPR and  $\mu$ SR experiments, respectively. The results are demonstrated in contour plots in Fig. 21. On the electron, one can observe the SQ transitions in addition to the MQ ones. The SQ transitions form the expected Pake pattern, while the MQ transitions form two ridges and are influenced substantially less by  $\theta$ . The muon polarization is only influenced by MQ tran-

sitions, therefore only showing their  $\theta$ -dependence. The MQ peaks are most intense at around  $\theta = 45^\circ$ , while there are no peaks observed at  $\theta = 0^\circ$  and  $\theta = 90^\circ$ . This is expected as those angles make the MQ transitions forbidden, resulting in no muon polarization being transferred to the electron.

The baseline is also  $\theta$  dependent, going as low as  $P_z^{\mu^+} = 0.75$  for  $\theta = 35^\circ$  with a maximum of  $P_z^{\mu^+} = 1$  for  $\theta = 0^\circ$  and  $\theta = 90^\circ$ . This is caused by the muon not being in the high-field limit at the simulated external magnetic fields  $B_0$ , which causes state mixing analogous to what is observed in Fig. 20a.

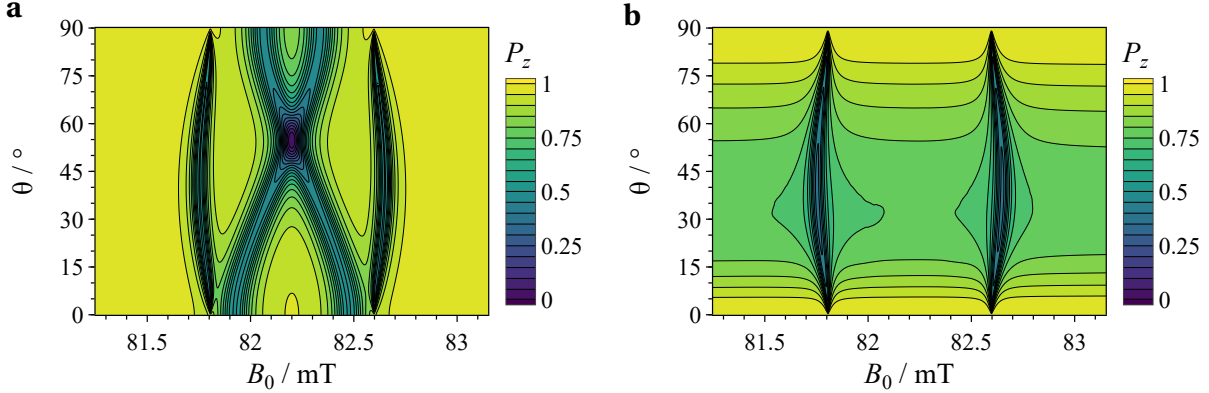


**Fig. 21:** Contour plots showing the  $\theta$ -dependence of the average electron (**a**) and muon (**b**) polarization in Mu as a function of the magnetic field during microwave irradiation. The initial polarizations were set as either  $P_z^{e^-} = 1$  and  $P_z^{\mu^+} = 0$  or vice versa, mimicking EPR and  $\mu$ SR experiments, respectively. The isotropic coupling constant was defined to be  $A_{\text{iso}} = 0$  MHz. See text for details on other parameters. (**a**) Both the SQ and MQ transitions can be seen, with the SQ transitions forming the Pake pattern. The MQ transitions give rise to the two ridges. Their  $\theta$ -dependence is less prominent. The MQ transitions are observable in both spectra, forming the same shape. Additionally, the base line also depends on  $\theta$  since the muon is not in the high-field limit, resulting in a polarization transfer to the electron.

### 4.3.2 $A_{\text{iso}}$ -Dependence

The transition probability of MQ transitions depends on the coupling constants  $A_{\text{iso}}$  and  $D_{\parallel}$  because they lead to tilting of the quantization axes. This is best seen via the direct relation to the secular hyperfine coupling constant  $A$  and pseudo-secular hyperfine coupling constant  $B$ , namely

$$A = A_{\text{iso}} + D_{\parallel}(3 \cos^2 \theta - 1) \quad \text{and} \quad B = 3D_{\parallel} \sin \theta \cos \theta . \quad (23)$$

To investigate the effect of  $A_{\text{iso}}$  on MQ- $\mu$ SR powder spectra, numerical simulations of Mu with different  $A_{\text{iso}}$  were carried out with the results shown in Fig. 22. As expected, the peak intensities and widths decrease with  $A_{\text{iso}}$ , since that decreases the tilting of the quantization axes. The effect of  $A_{\text{iso}}$  on the peak positions is small up to  $A_{\text{iso}} \geq 50$  MHz and shows no clear trend. After 50 MHz however, the first peak starts shifting to lower fields with decreased intensity compared to the second peak. No other trends are discernible in the effects of  $A_{\text{iso}}$  on the spectra. Further simulations with a finer  $A_{\text{iso}}$  grid could give additional insights into the nature of the  $A_{\text{iso}}$ -dependence.

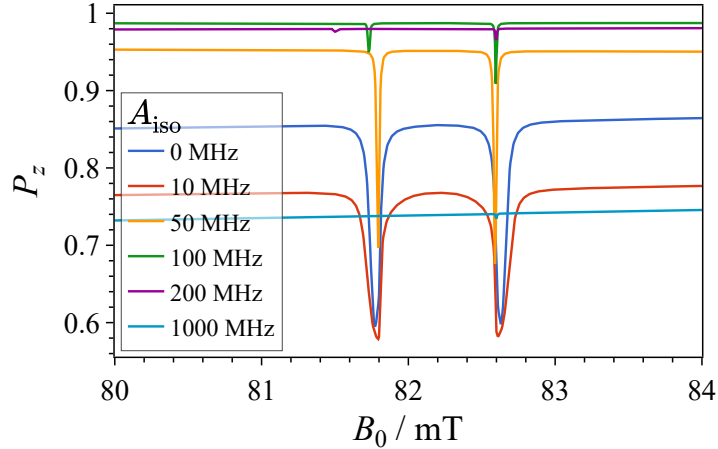


**Fig. 22:** Numerically simulated MQ-μSR powder spectra for Mu with different  $A_{\text{iso}}$ . The peak intensity decreases with  $A_{\text{iso}}$  due to the MQ transitions becoming formally less allowed. The impact on the peak positions is small up to  $A_{\text{iso}} \geq 50 \text{ MHz}$ , after which the first peak starts shifting to lower fields and decreased intensity compared to the second peak. Presumably, this results in the first peak not being in the simulated range for  $A_{\text{iso}} = 1000 \text{ MHz}$ , leaving only the second peak visible. The baseline is greatly influenced by  $A_{\text{iso}}$ , probably due to ALC resonances which are not in the simulated range.

### 4.3.3 $T_2^{\text{e}^-}$ -Dependence

It is already established by EPR spectroscopy that the transverse electron relaxation time  $T_2^{\text{e}^-}$  depends heavily on the interactions with the local environment. This can lead to relaxation times ranging from a few nanoseconds up to seconds in low-temperature experiments [9]. A short  $T_2^{\text{e}^-}$  leads to line broadening in EPR as well as in MQ-μSR powder spectra. The influence of  $T_2^{\text{e}^-}$  on line broadening in MQ-μSR powder spectra was studied by varying  $T_2^{\text{e}^-}$ , which was implemented phenomenologically by setting  $T_2$  of the MQ transitions to  $T_2^{\text{e}^-}$ . The resulting spectra are shown in Fig. 24. Two peaks are obtained for long  $T_2^{\text{e}^-}$ , which start to overlap with decreasing  $T_2^{\text{e}^-}$  until they become indistinguishable at  $T_2^{\text{e}^-} = 5 \text{ ns}$ . Note that typically  $T_2^{\text{e}^-} \gg 5 \text{ ns}$  with fast relaxation times being around  $T_2^{\text{e}^-} = 20 \text{ ns}$ . The results suggest that line shape analysis of MQ-μSR does not allow easy extraction of the hyperfine coupling constants by simple fitting for systems with short  $T_2^{\text{e}^-}$ . Numerical simulations including the effects of  $T_2^{\text{e}^-}$  would be needed to compute the hyperfine coupling constants.

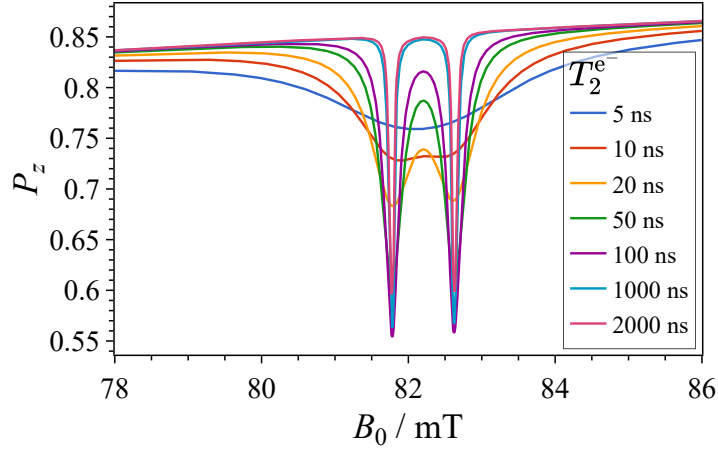


**Fig. 23:** Numerically simulated MQ powder spectra with different electron relaxation times  $T_2^{e-}$ . The two distinct peaks received for large  $T_2^{e-}$  merge into one broad peak for  $T_2^{e-} = 5 \text{ ns}$ . The peak broadening makes line shape analysis of MQ powder spectra to extract the hyperfine coupling constants more challenging.

#### 4.3.4 $\nu_1$ -Dependence

Increasing the power of the driving irradiation typically leads to an increase in signal intensity in nearly all spectroscopic fields, but it also results in line broadening. Numerical simulations were performed to investigate the influence of microwave irradiation amplitude  $\nu_1$  on MQ- $\mu$ SR powder spectra (Fig. 24). The polarization drop at the resonances almost doubles by increasing  $\nu_1 = 1 \text{ MHz}$  to  $10 \text{ MHz}$ . However, the peaks are also broadened to the point where they overlap. Further increasing  $\nu_1$  decreases the peak height and merges the two peaks into one. For  $\nu_1 \geq 30 \text{ MHz}$ , the polarization  $P_z$  starts to increase at the resonance instead of decreasing. This is caused by the driving Hamiltonian outweighing the interaction Hamiltonian, effectively decoupling the muon and electron [33]. The simulations suggest that  $\nu_1$  should be calibrated before MQ- $\mu$ SR measurements to ensure maximum signal-to-noise ratio, as choosing a large  $\nu_1$  will lead to a decrease in signal intensity. In experimental work one has to additionally consider that  $\nu_1$  should not be too large to avoid missing small couplings, while  $\nu_1$  needs to be large enough for a sufficient flip angle on  $T_2^{e-}$  scales, e.g.  $\nu_1 T_2^{e-} \sin^2 \eta \gg 1$ .

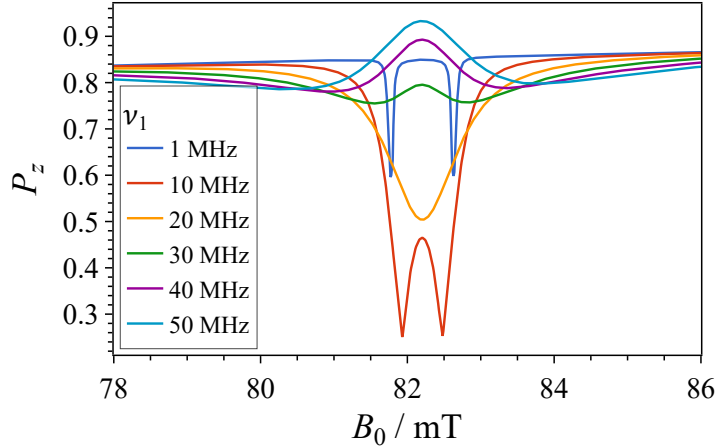


**Fig. 24:** Simulated MQ- $\mu$ SR powder spectra with different microwave irradiation amplitudes  $\nu_1$ . At first, increasing  $\nu_1$  increases the peak intensity but also results in line broadening. Further increasing  $\nu_1$  leads to additional line broadening, with the peak intensity starting to decrease. This results in an inversion of peak direction for  $\nu_1 \geq 30$  MHz, at which point the polarization  $P_z$  increases at the resonance.

#### 4.4 Muonium in Silicalite-1

Zeolites are microporous aluminosilicates with remarkable adsorption and catalytic activity [34–36]. They are widely used in industrial applications, beginning in the 1960s where the zeolite Y was used as a cracking catalyst in oil processing [37]. Arseneau et al. have shown via TF- $\mu$ SR that strongly-coupled Mu is formed as the initial state in multiple zeolites, including zeolite socony mobil-5 (ZSM-5) and silicalite-115 (S-115) [38]. In this work, the zeolite S-1 with very similar structure to ZSM-5 and S-115 was investigated via ZF-, TF- and MQ- $\mu$ SR. Note, that only the initially formed muon species can be observed with ZF and TF measurements, since not all delayed-formation states are created simultaneously. The interference of their signals causes the oscillations, needed for determining the muon species, to disappear. At first, as a reference, ZF spectra of SrTiO<sub>3</sub> were measured at 30 K and 70 K and are given in Fig. 25. SrTiO<sub>3</sub> was used because it has been shown to form weakly-coupled Mu as the initial state [10]. It is apparent from the ZF spectra that weakly-coupled Mu is only formed at 30 K, because the fast decay of  $A(t)$  at short  $t$  is an indicator for weakly-coupled Mu. The fast decay is caused by the powder averaging of the time-signals eliminating the oscillations, and a distribution of the hyperfine coupling constants that is only possible for weakly-coupled Mu. It is already established that no Mu is formed at 70 K, which is why it was used for reference [10].

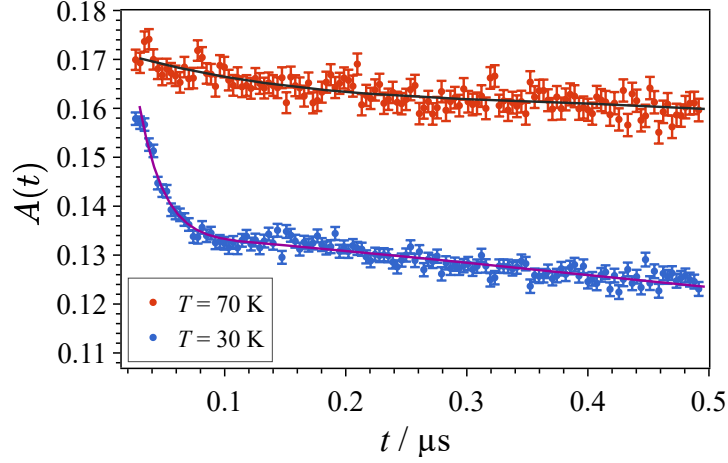


**Fig. 25:** TF- $\mu$ SR spectra of  $\text{SrTiO}_3$  measured at 30 K and 70 K focusing on the first 500 ns. The fast decay of  $A(t)$  at short  $t$ , which indicates the formation of weakly-coupled Mu, is only observed for  $T = 30 \text{ K}$ . It is caused by a distribution of hyperfine coupling constants and powder averaging of the time signals. The traces were fitted with a double exponential cosine. A bin size of 150 was chosen.

The ZF and TF spectra of S-1 measured at 260 K are displayed in Fig. 26a, with Fig. 26b showing a magnified view. The ZF spectrum leaves the possibility open that the initially formed Mu is weakly-coupled due to the fast initial decay of  $A(t)$ , which is also observed in  $\text{SrTiO}_3$ . However, the fast initial oscillations in the TF spectrum prove that the formed Mu is strongly coupled. These initial oscillations result from transitions between the triplet states. The extended, slow oscillations result from precession of the muon spin around  $B_0$ .

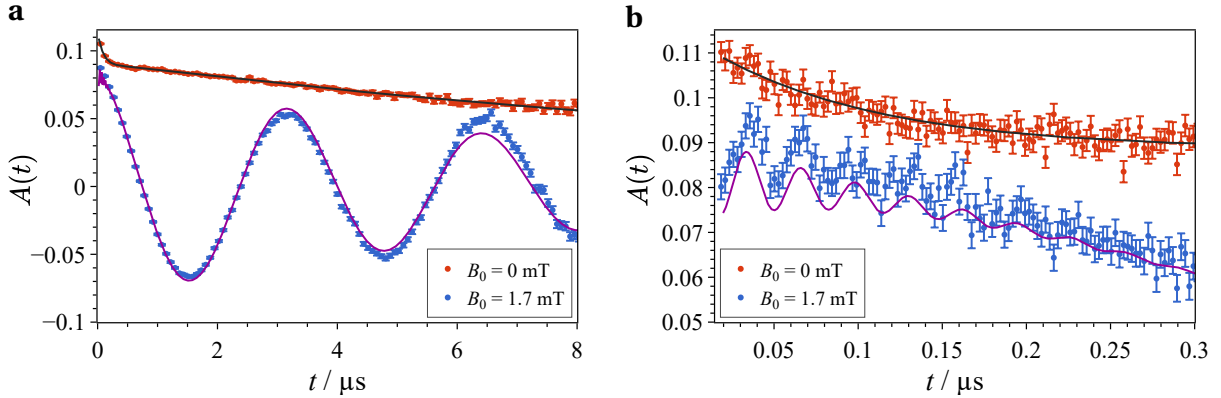


**Fig. 26:** ZF- and TF- $\mu$ SR spectra of the zeolite S-1 measured at 260 K. A bin size of 3000 is used for the full spectrum (a) and 100 for the magnified spectrum (b). The data was fitted using a double exponential cosine, which captures both the fast and slow oscillations in the TF spectrum. The presence of the fast oscillation for the TF measurements indicates that the initially formed Mu species is strongly coupled.

Nonetheless, MQ- $\mu$ SR measurements prove the delayed formation of weakly-coupled Mu, resulting in

a MQ resonance observed at  $B_0 = 128$  mT with microwave excitation of  $\nu_{\mu\text{w}} = 3.580$  GHz (Fig. 27). The weakly-coupled Mu is probably a reaction product of the strongly-coupled Mu, as the initial fraction of strongly-coupled Mu has relaxed at  $t = 300$  ns when the MQ measurement starts. The width of the resonance suggests line broadening caused by  $T_2^{\text{e}^-}$  and  $\nu_1$ , as only one broad peak is observed opposed to the expected two. In addition to the large resonance, two weak satellite resonances are visible at  $B_0 = 124$  mT and 131 mT. These points were remeasured for confirmation, with  $B_0 = 124$  mT being successfully used for the rotary spin echo experiments (Section 4.5), proving its presence. The reason for the side resonances is not known, but could be caused by interactions with a nucleus. Quantum chemical calculations of the muon site are needed for further investigation. The results support the viability of MQ- $\mu$ SR for observing delayed formation of weakly-coupled Mu in powder samples, making MQ- $\mu$ SR a further tool that can be used to monitor the evolution of Mu inside solids.

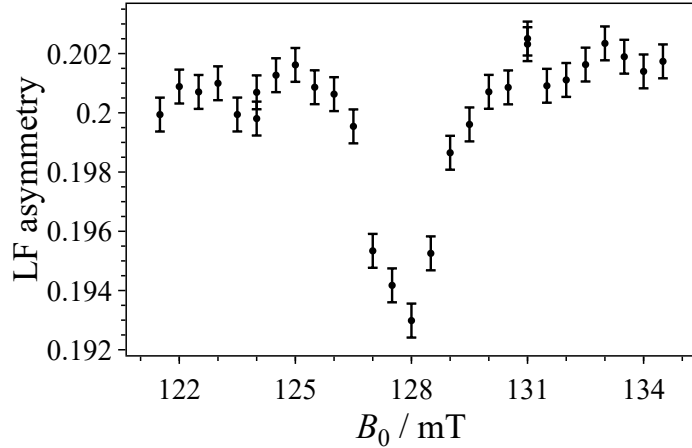


**Fig. 27:** MQ- $\mu$ SR spectrum of the zeolite S-1 measured at 260 K and microwave excitation of  $\nu_{\mu\text{w}} = 3.580$  GHz. The data points at  $B_0 = 124$  mT and 131 mT were measured twice to confirm the two features outside of the main peak at  $B_0 = 128$  mT. The MQ resonances prove the delayed formation of weakly-coupled Mu.

## 4.5 Rotary Spin Echos

Spin echo techniques are commonplace in NMR and EPR spectroscopy but have not gained much traction in  $\mu$ SR despite being studied in detail previously [39–41]. The rotary spin echo (or LF echo) is an echo technique, where the defocusing caused by  $B_0$ -field and  $B_1$ -field inhomogeneities as well as imperfect flip angles are refocused [42, 43]. This is done by a phase shift of  $\pi$  at time  $\tau/2$  (Fig. 28).

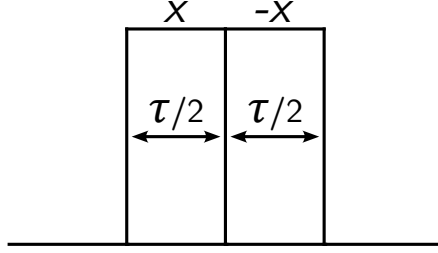


**Fig. 28:** Schematic depiction of the pulse sequence used to generate the rotary spin echo. The pulse has a total length of  $\tau$  with a phase shift of  $\pi$  at time  $\tau/2$ .

It should, in theory, increase the time signal intensity in MQ- $\mu$ SR measurements and thus enhance the peaks in the spectra. The impact of the rotary echo on MQ- $\mu$ SR spectra was investigated using S-1 as a sample. The LF asymmetry was measured as a function of the pulse length  $\tau$  for linear phase pulses and rotary echos (Fig. 29). The rotary echo increases the signal slightly for large  $\tau$  but has no effect on small  $\tau$ . The cutoff of the two regimes depends on the intensity of the pulse, as with 50 W microwave pulse power the cutoff is at  $\tau \approx 100$  ns (Fig. 29a). For experiments with 90 W pulse power, an increase in signal is already observed at  $\tau \approx 80$  ns (Fig. 29b). The absolute signal improvements gained with the rotary echo are rather small but one has to keep in mind that the effects, which are studied in MQ- $\mu$ SR, can be tiny, as seen in Fig. 27. The limiting factor for the signal increase is  $T_2^{e^-}$ , as the signal intensity is proportional to  $\exp\left(-\frac{t}{T_2}\right)$  [9]. For most samples with temperatures close to ambient temperature,  $T_2$  is in the ns range, capping the potential signal increase with the rotary echo. Comparing the LF asymmetry decrease using the two different pulses for very short  $\tau$  with the LF asymmetry decrease for longer  $\tau$  gives an estimate on the potential signal increase in MQ- $\mu$ SR spectra. This was crudely approximated to be  $\approx 30\%$  for the measurements with 50 W pulse power and  $\approx 90\%$  for the high power 90 W pulse. Considering that the experimental realization of rotary spin echos poses no significant challenge, no major downside exists to using them for MQ- $\mu$ SR measurements.

Similar improvements to the absolute signal intensity could be gained by changing from one-muon-at-a-time to time-integral acquisition, where up to 100 times larger muon rates are possible. In time-integral acquisition, only the total counts of the positron detectors are used to determine the asymmetry, at the expense of any temporal resolution of the asymmetry. Currently, one MQ- $\mu$ SR data points takes about 1 hour to measure. In contrast, an ALC- $\mu$ SR data point with a significantly smaller error is measured in under one minute with time-integral acquisition [44]. Therefore, in future, MQ- $\mu$ SR should also employ time-integral acquisition, but additional development of the experimental setup is needed, as the microwave irradiation has to be pulsed to prevent severe heating of the sample.

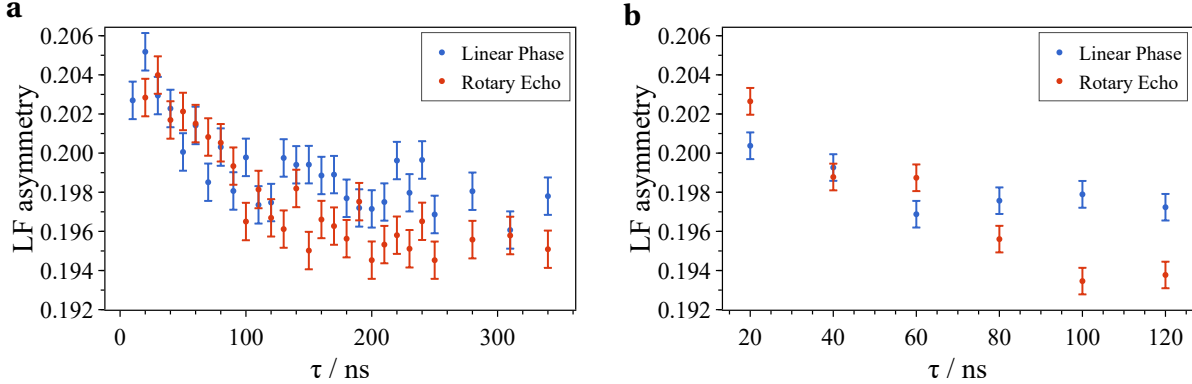


**Fig. 29:** The experimental LF asymmetry as a function of the total pulse length  $\tau$  for linear phase pulses and the rotary echos. The measurements were conducted using 50 W (a) and 90 W pulses (b), respectively. The rotary echo leads to a larger signal starting from around  $\tau = 100$  ns for the 50 W pulse. Increasing the microwave power results in an enhanced signal for both pulse types and also an increased difference starting at  $\tau = 80$  ns. The rotary echo causes a signal increase of  $\approx 90\%$  for high power which, in the context of MQ- $\mu$ SR approaches where the changes in LF asymmetry are small, is worth the added experimental effort.

In a further experiment on S-1, the rotary echo LF asymmetry was compared to measurements with no microwave excitation. The results are displayed in Fig. 30. For the rotary echo, the total pulse length was set to  $\tau = 100$  ns with a frequency of  $\nu_{\mu\text{W}} = 3.580$  GHz. All measurements were carried out at 260 K. The goal was to test the time stability of the setup and further examine the small resonance observed at  $B_0 = 124$  mT in the MQ- $\mu$ SR powder spectrum in Fig. 27. The experiment further confirms the presence of the resonance at  $B_0 = 124$  mT, as only a decrease in LF asymmetry is observed for  $B_0 = 124$  mT, but not for  $B_0 = 125$  mT. A drift over time is recognizable with and without microwave excitation, but successive points still confirm the presence of the resonance. This suggests that the absolute LF asymmetries of MQ- $\mu$ SR spectra cannot be compared to later measurements, but data collected in a reasonable time frame still allows the determination of resonances. Further experiments on the drift over time are needed to fully characterize the extent and to test possible ways to mitigate the drift.

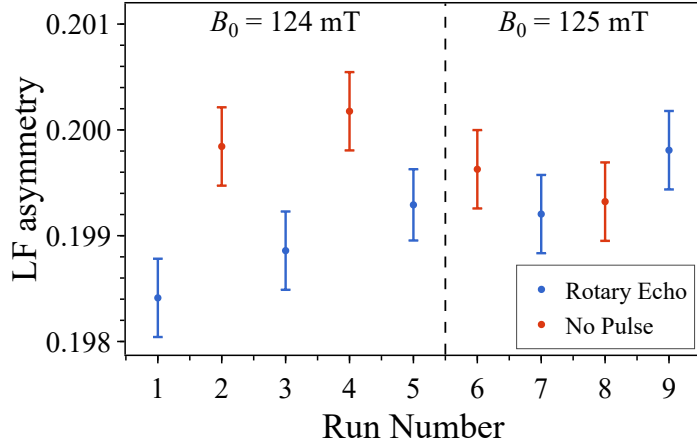


**Fig. 30:** LF asymmetry measurements with and without microwave excitation of S-1 at 260 K with  $B_0 = 124 \text{ mT}$  or  $B_0 = 125 \text{ mT}$  (separated by dashed line).  $\tau = 100 \text{ ns}$  was chosen based on Fig. 29 with a frequency of  $v_{\mu\text{w}} = 3.580 \text{ GHz}$ . A drift over time is visible, but the resonance at  $B_0 = 124 \text{ mT}$  can still be discerned by comparing successive measurements.  $B_0 = 125 \text{ mT}$  shows no resonance as microwave excitation has no clear effect on the LF asymmetry.

## 5 Conclusion & Outlook

The potential application of ALC- $\mu$ SR to investigate powder samples, which form weakly-coupled Mu, was investigated using numerical spin dynamics simulations. The resulting spectra establish that the ALC resonances are close to ZF for weakly-coupled Mu, resulting in overlap with the muon repolarization. This results in an interesting  $\theta$ -dependence of the spectra, showing similarities to the Pake pattern, which is distorted from the muon repolarization. The distortion makes ALC- $\mu$ SR an impractical method for characterizing weakly-coupled Mu in powder samples, as extensive numerical simulations would be needed to analyze ALC powder spectra.

We show that MQ- $\mu$ SR is a viable method for detecting delayed formation of weakly-coupled Mu in powder samples. The MQ spectrum of S-1 was measured, proving the presence of weakly-coupled Mu due to the three resonances observed at  $B_0 = 124 \text{ mT}$ ,  $128 \text{ mT}$  and  $131 \text{ mT}$ , respectively. The reason for the side bands is unknown and needs to be studied using quantum chemical calculations at the muon site for interpretation. ZF and TF measurements confirm that the initial state formed after implantation of the muon is strongly-coupled Mu. This suggests that weakly-coupled Mu is a reaction product of strongly-coupled Mu, because the initial fraction of strongly-coupled Mu has relaxed at  $t = 300 \text{ ns}$  when the MQ measurement begins. The results demonstrate that MQ- $\mu$ SR is a viable method to detect weakly-coupled Mu in powder samples, even if their formation is delayed. For future work, this allows to investigate reactions of Mu in powders, in which weakly-coupled Mu is formed. The effect of  $\theta$ ,  $A_{\text{iso}}$ ,  $T_2^{\text{e}^-}$  and  $v_1$  on the MQ spectrum was examined by numerical simulations. The potential increase in signal intensity of

rotary spin echos was investigated on the  $B_0 = 124$  mT resonance, further confirming its existence. The rotary echo was found to slightly improve the absolute signal intensity, but lead to a maximal relative signal increase of  $\approx 90\%$ . Its experimental implementation is not a major challenge and it should therefore be utilized in future MQ- $\mu$ SR work. The measured rotary echo data revealed a drift over time in the retrieved LF asymmetry value. This effect should be investigated in subsequent studies, as it could lead to signal improvements of similar magnitude than the rotary echo.

## References

- [1] P. J. Mohr, D. B. Newell, B. N. Taylor, E. Tiesinga, *Rev. Mod. Phys.* **2025**, *97*, 025002.
- [2] A. D. Hillier, S. J. Blundell, I. McKenzie, I. Umegaki, L. Shu, J. A. Wright, T. Prokscha, F. Bert, K. Shimomura, A. Berlie, H. Alberto, I. Watanabe, *Nat. Rev. Methods Primers* **2022**, *2*, 4.
- [3] S. Cottrell, C. Johnson, S. Cox, C. Scott, *Phys. B* **2003**, *326*, 248–251.
- [4] M. H. Dehn, Y. Cao, P.-X. Wang, S. P. Cottrell, M. J. MacLachlan, D. G. Fleming, R. F. Kiefl, *J. Chem. Phys* **2020**, *152*, 184706.
- [5] I. McKenzie, V. L. Karner, R. Scheuermann, *Quantum Beam Sci.* **2024**, *8*, 15.
- [6] J.-C. Brodovitch, S.-K. Leung, S. Sun-Mack, P. W. Percival, D. Yu, S. F. J. Cox, *Hyperfine Interact.* **1991**, *65*, 937–938.
- [7] D. Vujošević, H. Dilger, I. McKenzie, A. Martyniak, R. Scheuermann, E. Roduner, *J. Phys. Chem. B* **2007**, *111*, 199–208.
- [8] A. Doll, C. Wang, T. Prokscha, J. Dreiser, Z. Salman, *Phys. Rev. Res.* **2025**, *7*, 033059.
- [9] A. Schweiger, G. Jeschke, *Principles of Pulse Electron Paramagnetic Resonance*, Oxford University Press, **2001**.
- [10] T. U. Ito, W. Higemoto, A. Koda, K. Shimomura, *Appl. Phys. Lett.* **2019**, *115*, 192103.
- [11] Z. Salman, T. Prokscha, A. Amato, E. Morenzoni, R. Scheuermann, K. Sedlak, A. Suter, *Phys. Rev. Lett.* **2014**, *113*, 156801.
- [12] S. Navas et al., *Phys. Rev. D* **2024**, *110*, 030001.
- [13] A. Soter, “Introduction to Nuclear and Particle Physics”, lecture notes, ETH Zurich, **2025**.
- [14] D. G. Fleming, I. McKenzie, P. W. Percival, *Muon Spin Spectroscopy: Methods and Applications in Chemistry and Materials Science*, 1st ed., Wiley, **2024**.
- [15] A. Amato, E. Morenzoni, *Introduction to Muon Spin Spectroscopy: Applications to Solid State and Material Sciences*, Springer International Publishing, Cham, **2024**.
- [16] M. H. Levitt, *Spin Dynamics Basics of Nuclear Magnetic Resonance*, John Wiley & Sons, Ltd, **2012**.
- [17] S. J. Blundell, *Chem. Rev.* **2004**, *104*, 5717–5736.

- [18] E. Roduner, I. D. Reid, M. Riccò, R. D. Renzi, *Ber. Bunsen-Ges. Phys. Chem.* **1989**, *93*, 1194–1197.
- [19] I. McKenzie, V. L. Karner, R. Scheuermann, *Quantum Beam Science* **2024**, *8*, Publisher: Multidisciplinary Digital Publishing Institute, 15.
- [20] A. Amato, H. Luetkens, K. Sedlak, A. Stoykov, R. Scheuermann, M. Elender, A. Raselli, D. Graf, *Rev. Sci. Instrum.* **2017**, *88*, 093301.
- [21] A. Stoykov, R. Scheuermann, K. Sedlak, J. Rodriguez, U. Greuter, A. Amato, *Phys. Procedia* **2012**, *30*, 12th International Conference on Muon Spin Rotation, Relaxation and Resonance (SR2011), 7–11.
- [22] Product page of the silicalite-1 zeolite sample (type P-1500s), ACS Material, <https://www.acsmaterial.com/zsm-5-series-zeolite-powder.html> (visited on Jan. 27, 2026).
- [23] Product page of the SrTiO<sub>3</sub> sample, Sigma Aldrich, <https://www.sigmaaldrich.com/CH/de/product/aldrich/396141> (visited on Jan. 27, 2026).
- [24] The MathWorks Inc., *MATLAB versions R2024a & R2025b*, Available at [www.mathworks.com](http://www.mathworks.com).
- [25] S. Pribitzer, A. Doll, G. Jeschke, *J. Magn. Reson.* **2016**, *263*, 45–54.
- [26] Python Software Foundation, *Python version 3.13*, Available at [www.python.org](http://www.python.org).
- [27] N. Lambert, E. Giguère, P. Menczel, B. Li, P. Hopf, G. Su'arez, M. Gali, J. Lishman, R. Gadhvi, R. Agarwal, A. Galicia, N. Shammah, P. Nation, J. R. Johansson, S. Ahmed, S. Cross, A. Pitchford, F. Nori, *Phys. Rep.* **2026**, *1153*, 1–62.
- [28] C. R. Harris et al., *Nature* **2020**, *585*, 357–362.
- [29] H. W. Kuhn, *Nav. Res. Logist. Q.* **1955**, *2*, 83–97.
- [30] OpenAI, *ChatGPT (GPT-5 and GPT-4o)*, Available at <https://www.openai.com>, **2025**.
- [31] GitHub, Inc., *GitHub Copilot (GPT-4.1 Copilot)*, Available at <https://github.com/features/copilot>, **2025**.
- [32] I. McKenzie, R. Scheuermann, S. P. Cottrell, J. S. Lord, I. M. Tucker, *J. Phys. Chem. B* **2013**, *117*, 13614–13618.
- [33] J. S. Lord, *Phys. B* **2003**, *326*, 128–132.
- [34] N. Kordala, M. Wyszkowski, *Molecules* **2024**, *29*, 1069.
- [35] R. A. Schoonheydt, P. Geerlings, E. A. Pidko, R. A. van Santen, *J. Mater. Chem.* **2012**, *22*, 18705–18717.
- [36] A. Walkowiak, J. Wolska, A. Wojtaszek-Gurdak, I. Sobczak, L. Wolski, M. Ziolek, *Materials* **2021**, *14*.
- [37] P. Bai, U. J. Etim, Z. Yan, S. Mintova, Z. Zhang, Z. Zhong, X. Gao, *Catal. Rev.* **2019**, *61*, 333–405.
- [38] D. Arseneau, D. Fleming, C. Fyfe, M. Senba, *Phys. B* **2003**, *326*, 64–67.
- [39] S. R. Kreitzman, D. L. Williams, N. Kaplan, J. R. Kempton, J. H. Brewer, *Phys. Rev. Lett.* **1988**, *61*, 2890–2893.

- [40] S. R. Kreitzman, *Hyperfine Interact.* **1991**, *65*, 1055–1069.
- [41] N. J. Clayden, S. P. Cottrell, I. McKenzie, *J. Magn. Reson.* **2012**, *214*, 144–150.
- [42] A. J. Wheaton, G. R. Dodge, A. Borthakur, J. B. Kneeland, H. R. Schumacher, R. Reddy, *J. Orthop. Res.* **2005**, *23*, 102–108.
- [43] W. R. Witschey, A. Borthakur, M. A. Elliott, E. Mellon, S. Niyogi, C. Wang, R. Reddy, *Magn. Reson. Med.* **2007**, *57*, 2–7.
- [44] A. Stoykov, R. Scheuermann, K. Sedlak, T. Shiroka, V. Zhuk, *Phys. B* **2009**, *404*, 986–989.